



HAL
open science

Seawater paleotemperature and paleosalinity evolution in neritic environments of the Mediterranean margin: insights from isotope analysis of bivalve shells

Justine Briard, Emmanuelle Pucéat, Emmanuelle Vennin, M. Daëron, V. Chavagnac, R. Jaillet, Didier Merle, Marc de Rafélis

► To cite this version:

Justine Briard, Emmanuelle Pucéat, Emmanuelle Vennin, M. Daëron, V. Chavagnac, et al.. Seawater paleotemperature and paleosalinity evolution in neritic environments of the Mediterranean margin: insights from isotope analysis of bivalve shells. *Palaeogeography, Palaeoclimatology, Palaeoecology*, 2020, 543, pp.109582. 10.1016/j.palaeo.2019.109582 . hal-02449079

HAL Id: hal-02449079

<https://hal.science/hal-02449079v1>

Submitted on 22 Jun 2021

HAL is a multi-disciplinary open access archive for the deposit and dissemination of scientific research documents, whether they are published or not. The documents may come from teaching and research institutions in France or abroad, or from public or private research centers.

L'archive ouverte pluridisciplinaire **HAL**, est destinée au dépôt et à la diffusion de documents scientifiques de niveau recherche, publiés ou non, émanant des établissements d'enseignement et de recherche français ou étrangers, des laboratoires publics ou privés.

26 understand the behavior of our climate system during this critical interval. In this work, we
27 test the potential of a multi-proxy approach ($\delta^{18}\text{O}$, clumped isotope (Δ_{47}), strontium isotopes
28 ($^{87}\text{Sr}/^{86}\text{Sr}$)) applied to bivalves recovered from the Liguro-Provencal Basin and Rhodano-
29 Provencal basin (Northwestern of the Mediterranean Sea) to reconstruct the evolution of
30 shallow seawater temperature and salinity in this region over the latest Oligocene to Middle
31 Miocene interval (~10 Myrs). Our results highlight a local cooling in the northwestern
32 Mediterranean Sea during the MMCO that contrasts with the warming observed in other
33 regions, with seawater temperatures inferred from Δ_{47} analyses in the 13-18°C range. These
34 cool seawater temperatures recorded in the studied region during the MMCO are much cooler
35 than those recorded in the open oceans, but are in agreement with the proliferation of
36 bryozoan observed in the Castillon-Du-Gard area during this interval. Low bivalve $\delta^{18}\text{O}$
37 values (-3.24 ‰ in average) are recorded during this episode—are interpreted to reflect
38 enhanced freshwater inputs, lowering local salinity and seawater $\delta^{18}\text{O}$. Such enhanced
39 freshwater inputs point to a phase of enhanced hydrological cycle in the studied region,
40 possibly linked to the global mid-Miocene warming event. Bivalve $^{87}\text{Sr}/^{86}\text{Sr}$ data mostly fall
41 within the global seawater Sr isotope reference curve, but remain compatible with enhanced
42 freshwater inputs during the Aquitanian and during the Langhian, as these inputs were
43 probably not important enough to induce a large departure from the seawater curve at a
44 regional scale.

45

46

47 **Highlights :**

- 48 • Coupled Δ_{47} - $\delta^{18}\text{O}$ - $^{87}\text{Sr}/^{86}\text{Sr}$ analyses of bivalve shells decipher temperature and
49 salinity.

50 • Cool seawater temperatures in the northwestern Mediterranean Sea during the
51 MMCO.

52 • Enhanced hydrological cycle in western Europe during the MMCO.

53

54 **Keywords:** Paleoclimate; Middle Miocene Climatic Optimum; Clumped isotopes;
55 Hydrological cycle; Coastal environment

56

57 **1. Introduction**

58 A major feature of the long-term climate evolution during the Cenozoic is the
59 transition from the “greenhouse” conditions of the late Early Eocene (~50 million years ago)
60 to the modern “icehouse” climate mode with its much lower atmospheric CO₂ levels and
61 permanent polar ice-sheets on both poles (Zachos et al., 2008). This transition occurred
62 through a series of steps, beginning with the abrupt global cooling recorded at the
63 Eocene/Oligocene transition (Zachos et al., 1996; Lear et al., 2008; Liu et al., 2009; Galeotti
64 et al., 2016; Cramwinckel et al., 2018) followed by a period of instability of the Antarctic ice-
65 sheet during the Oligocene and part of the Miocene (Billups and Schrag, 2002; Lear et al.,
66 2015; Gasson et al., 2016). This period of instability is marked by several warming and
67 cooling phases associated with waxing and waning of the Antarctica ice-sheet. This includes
68 the Late Oligocene Warming Event, the cooling at the Oligocene-Miocene boundary (~23.03
69 Ma, Mi-1 event), and the global warming event leading to the Middle Miocene Climatic
70 Optimum (MMCO, ca. 16 Ma to ca. 14.5 Ma) during the latest Early to Middle Miocene
71 interval (e.g. Zachos et al., 2008; Mawbey and Lear, 2013; Beddow et al., 2016, Goldner et
72 al., 2014; Holbourn et al., 2015; Super et al., 2018). This phase of instability ended with the
73 marked cooling of sea surface temperature (SST) defined as the Middle Miocene Climate
74 Transition (MMCT, ca. 14.5 to ca. 13.5 Ma), associated once more with a large-scale

75 expansion of the Antarctic ice-sheet (Holbourn et al., 2005; Foster et al., 2012). Although the
76 first development of permanent ice-sheets on Antarctica during the Eocene-Oligocene cooling
77 event has been extensively studied in the past decades (Zachos et al., 1996; Ivany et al., 2000;
78 Lear et al., 2008; Liu et al., 2009; Tremblin et al., 2016), little is known about the following
79 interval of ice-sheet instability. For the earliest Oligocene to the middle Miocene interval (~
80 10 million years), most paleoclimatic records available to date are based on isotopic ($\delta^{18}\text{O}$)
81 and elemental (Mg/Ca) composition of benthic foraminifera that record the physico-chemical
82 features of ocean bottom water temperature (Pagani et al., 1999; Miller et al., 1991; Diester-
83 Haass et al., 2009). Marine surface temperature records are scarce, mostly based on various
84 geochemical measurements on planktonic organisms (e.g. $\delta^{18}\text{O}$, Mg/Ca, TEX_{86} , U_{37}^{kl}), and are
85 restricted to limited time intervals (Pagani et al., 1999; Super et al., 2018). Palynological data
86 or fauna distribution give further information on paleoenvironmental conditions on the
87 continents. (Bruch et al., 2004; Jimenez and Suc 2007; Pound et al., 2012). However, archives
88 from coastal environments such as bivalves remain understudied for this time period despite
89 their location in a transitional environment between continent and ocean important to
90 characterize as well to obtain a global view of the response of climate to perturbations.
91 Bivalves recovered from shallow-water environments (< 50 m, Stenzel, 1971) have been
92 successfully used to document temperature and/or salinity variations in the past (Klein et al.,
93 1996; Kirby et al., 1998, Steuber et al., 2005; Schöne and Giere 2005; Huyghe et al., 2012,
94 2015; Bougeois et al., 2014, 2016; Mouchi et al., 2018; de Winter et al., 2018). Bivalves like
95 oyster shells offer key advantages for paleotemperature reconstructions in coastal area, as (1)
96 they are formed of low-magnesian calcite, thus quite resistant to recrystallization (Brand and
97 Veizer, 1981; Al-Aasm and Veizer, 1986; Ulmann and Korte, 2015), (2) they have a large
98 spatial and temporal distribution and (3) they live fixed on a substratum during several years,
99 allowing reconstruction of local seasonal variations of environmental parameters (temperature

100 and salinity), which cannot be assessed with foraminifera. In coastal environments,
101 reconstruction of shallow water temperatures using bivalve $\delta^{18}\text{O}$ can however be impeded by
102 local seawater $\delta^{18}\text{O}$ ($\delta^{18}\text{O}_{\text{sw}}$) variability due to local processes such as evaporation,
103 precipitation, surface runoff and groundwater discharges. One way to overcome this limitation
104 is to combine conventional oxygen isotope ($\delta^{18}\text{O}$) with clumped isotope (Δ_{47}) analyses of
105 bivalves because carbonate clumped isotope (Δ_{47}) composition is solely linked to temperature
106 during mineral formation, and independent from the isotopic composition of the ambient
107 water (Ghosh et al., 2006; Schauble et al., 2006; Eiler et al., 2009; Henkes et al., 2013).
108 Additional information on environmental conditions is provided by the Sr isotopic system
109 applied on bivalves, as the $^{87}\text{Sr}/^{86}\text{Sr}$ ratios recorded in their umbo has been shown to record
110 the occurrence of large freshwater discharge in their living marine environment (Ingram and
111 Sloan, 1992; Bryant et al., 1995; Winderlund and Anderson, 2006; El Meknassi et al., 2018;
112 Zaky et al., 2018).

113 In this context, we propose to test the potential of a multi-proxy approach applied on
114 bivalves thriving in coastal environments to reconstruct the evolution of shallow (<50m)
115 seawater temperatures over the latest Oligocene to Middle Miocene interval. The two selected
116 outcrops, i.e. Carry-Le-Rouet and Castillon-Du-Gard located within the Liguro-Provencal and
117 Rhodano-Provencal Basins (SE of the Mediterranean Sea, France), present sediments
118 deposited in shallow (<50m) open marine conditions with abundant bivalve shells. In both
119 localities, a well-constrained chronostratigraphic framework is available (Andrieieff et al.,
120 1972; Oudet et al., 2010; Ferrandini et al., 2010; Demory et al., 2011). Our new dataset
121 provides new information on both temperature, salinity and runoff evolution within a still
122 understudied region. The outcomes contribute to better constrain the regional environmental
123 response to global climatic changes during this key interval of Antarctica ice-sheet waning
124 and waxing.

125

126 **2. Geological setting**

127 The modern western Mediterranean Sea is structured into four basins (Fig.1A):
128 Alboran Sea, Adriatic Sea, Tyrrhenian Sea, and Liguro-Provençal basin that extends from the
129 Gulf of Genoa in the East to the Strait of Gibraltar in the West to Sardinia in the South. These
130 basins began to form by the end of the Oligocene (~23.03 Ma) and reached their full
131 extension during the Miocene (23.03 – 5.33 Ma) (Rehault et al., 1984). The oceanization of
132 the Liguro-Provençal basin corresponds to the opening of a back-arc basin associated with the
133 eastward retreat of an Adriatic/ionian slab sinking into the mantle (Gueguen et al., 1998;
134 Faccenna et al., 1997; Gattacceca et al., 2007; van Hinsbergen et al., 2019). During the
135 Miocene marine transgression, a second basin started to form in the Rhône Valley, called the
136 Rhodano-Provençal Basin. This basin is located north of the Liguro-Provençal Basin, at the
137 junction between the perialpine foreland basin to the north and the northern margin of the
138 western Mediterranean to the south. The Rhodano-Provençal Basin extends to the north as a
139 channel that follows the alpine chain from Marseille (France) to Vienna (Austria). The pre-
140 Miocene structuration of the Rhodano-Provençal Basin results in a highly differentiated
141 topography organized in sub-basins (e.g. Valreas, Sommières, Uzès and Castillon-Du-Gard).
142 Due to this inheritance, the Rhodano-Provençal sub-basins evolved independently of each
143 other during the Miocene marine transgression. The two outcrops selected for this study are
144 located within the Liguro-Provençal (Carry-Le-Rouet) and Rhodano-Provençal (Castillon-Du-
145 Gard) basins (Fig. 1A).

146

147 *2.1. Carry-Le-Rouet outcrops in the Coastal Nerthe area*

148 On the northern part of the Liguro-Provençal Basin (Fig. 1B), a ~100 m succession of
149 Late Oligocene (Chattian) to Early Miocene (Burdigalian) continental and marine sediments

150 crops out along the Blue coast (43°19'50.19''N, 5°09'05.67''E), at Carry-Le-Rouet (20 km
151 west of Marseille, France). The sedimentary succession is separated by a major unconformity
152 from the deformed and eroded Mesozoic basement called Nerthe Massif. The Barrémo-Aptian
153 basement (Urgonian facies) is a thrust structure resulting from the Eocene Pyrenean
154 compression (Tempier, 1987). The outcrops are exposed along the coast on 8 km and the
155 sediments are organized in six lithostratigraphic units extending from the Cap de Nautès to
156 the Pointe de Tamaris (Fig. 1B; Andreieff et al., 1972; Maurel-Ferrandini, 1976). The basal
157 Conglomeratic Rouet unit (Unit 1, Chattian) is characterized by a transition from fluvial to
158 deltaic depositional environments. The following formations (Para-reefal Cap de Nautès unit
159 (Unit 2), the Brackish Rousset unit (Unit 3), the Bioclastic Carry unit (Unit 4), the Biodetrital
160 Sausset unit (Unit 5) and the Plan de Sausset unit (Unit 6)) correspond to an alternation of
161 marine to continental-marine transitional depositional environments. This succession benefits
162 from a well-constrained biostratigraphic record using calcareous nannofossils and planktonic
163 foraminifera (Oudet et al., 2010), supplemented with magnetostratigraphy (Demory et al.,
164 2011). Despite the presence of hiatus along the Chattian to Burdigalian succession, the
165 interval sampled in this study did not record any major stratigraphic gaps considering the
166 sedimentary succession continuity and the age model proposed by Demory et al., 2011.

167

168 *2.2. Castillon-Du-Gard outcrops*

169 The Castillon-Du-Gard Sub-basin (43°58'12.61''N, 4°33'16.05''E) of the Rhodano-
170 Provencal Basin (Fig. 1C) presents marine deposits of lower to middle Miocene in age
171 (Demarcq, 1970). This Sub-basin rests above a thick Mesozoic succession in a corridor and is
172 separated from the main Rhodanian basin by the N040° Nîmes Fault (Reynaud et al., 2012).
173 The sediments are organized into five lithostratigraphic formations (Greenish Molasse, Saint-
174 Siffret Marls, Uzès Molasse, Blue Marls and Castillon Molasse, respectively) ranging from

175 the Burdigalian to the regional “Helvetian” stage (Langhian-Serravallian equivalent; Fig. 1C).
176 Only “Helvetian” stage is presented here, which is in temporal continuity with the Carry-Le-
177 Rouet outcrops. The Helvetian stage at Castillon-Du-Gard Sub-basin is organized into two
178 distinct formations (Fm.): the blue marls at the base and the Castillon Molasse at the top. The
179 blue marls Fm. varies laterally in thickness from a few meters to 70 m-thick. They consist
180 mainly of lithoclasts composed of calcite, feldspar, glauconite, muscovite and iron oxide grain
181 and planktonic and benthic foraminifera, echinoderms, bryozoans and mollusks (Reynaud et
182 al., 2012). The Castillon Molasse is about 70 m-thick and is composed of a bryozoan and
183 mollusk packstone-rudstone (Bryomol; Reynaud et al., 2012). It is subdivided into two sub-
184 formations: the Vers Unit at the base and the Castillon Unit s.s at the top. The presence of
185 glauconite and oxide of iron in the Vers unit gives a characteristic yellow color to the
186 Bryomol packstone rich in pectenids encrusted by oysters, barnacles and bryozoans. Castillon
187 Unit s.s is a Bryomol floatstone differs from the Vers Unit by the occurrence of green and red
188 algae (Reynaud et al., 2012).

189 The depositional setting corresponds to an offshore environment for the Blue Marls,
190 protected from currents and waves. The Castillon Molasse is interpreted as being deposited in
191 a shallow tidal bay (Reynaud et al., 2012). The stability and homogeneity of the floro-faunal
192 assemblages throughout the whole sedimentary succession are indicative of open marine
193 conditions without major variation in salinity Reynaud et al., 2012).

194 Several hundred oyster shells were collected on about thirty different levels of the
195 Carry-Le-Rouet section. All these oysters belong to the *Ostrea* genus and some have been
196 determined to be *Ostrea fimbriata* species. A hundred oyster shell fragments were collected
197 on about twenty different levels for the Castillon-Du-Gard section, unfortunately the sample
198 size did not allow the species identification.

199

200 **3. Materials and methods**

201 *3.1. Preservation of the studied material*

202 Each oyster shell was embedded in Araldite ® 2020 resin from Huntsman (Basel,
203 Switzerland), sawed perpendicularly to growth lines along the major growth axis (Fig. 2A),
204 and carefully polished. Polished sections were observed under cathodoluminescence
205 microscopy (CL) to assess the preservation state of each shell. CL analyses were carried out
206 on a luminoscope (ELM – 3R) coupled to LEICA MZ12 microscope surmounted by a camera
207 Lumenera Infinity 3. Luminescent areas with large unorganized calcite crystals (mainly
208 chalky areas that are more sensitive to recrystallization; Kirby et al., 1998; Lartaud et al.,
209 2006; Ulmann et al., 2013; de Winter et al., 2018) and non-luminescent to weakly
210 luminescent areas with identifiable seasonal patterns of growths (Fig. 2B) of each shell
211 section were precisely mapped. The luminescent areas are representative of recrystallized
212 calcite and have not been sampled for isotopic analyses. Only the non-luminescent to weakly
213 luminescent parts of the shells, where a slight luminescence follows the seasonal patterns of
214 growths (induced by natural incorporation of Mn^{2+} in calcitic structure; Langlet et al., 2006),
215 have been sampled for $\delta^{18}O$, Δ_{47} and $^{87}Sr/^{86}Sr$ analyses, according to recent works (Lartaud et
216 al., 2010; Huyghe et al., 2015; Bougeois et al., 2016). The Carry-le-Rouet and Castillon-Du-
217 Gard outcrops only encountered a shallow burial (<100 m; Reynaud et al., 2006; Hamon et
218 al., 2013; Seibel and James, 2017) as evidenced by the absence of compaction traces and the
219 absence of younger sediment deposition in the region. Such shallow burial depths (Choquette
220 and James, 1990) ensures that the sediments have not encountered large overburden pressure
221 or elevated temperatures. This argues for an absence of solid-state reordering in the analyzed
222 bivalve shells and therefore a preservation of initial Δ_{47} signal.

223

224 *3.2. Oxygen isotope analyses*

225 For this study, 534 samples were recovered from 101 shells. For most of the shell
226 fragments, 1 to 3 different powder sample have been collected, each of them by gathering
227 carbonate powder along a transect perpendicular to the growth line of the individual shell, in
228 order to average the $\delta^{18}\text{O}$ value over at least part of the oyster life and minimize the variability
229 within and between shells from a single stratigraphic level. For 6 of the largest oyster shells, a
230 microsampling along a transect perpendicular to the growth lines was performed in the
231 ligamental area (Fig. 2A) to assess the variability of isotopic signal during at least part of the
232 bivalve life. For these shells, the $\delta^{18}\text{O}$ value of each measurement along this transect is
233 reported on Suppl. Table 1 in bold. The recovered powders were analyzed for its oxygen
234 isotope composition : 30 to 40 μg of calcite collected using a scalpel reacted with 100 %
235 phosphoric acid at 70 °C using a KIEL IV Carbonate Device connected to a Delta V Plus
236 Isotope ratio mass spectrometer at the Biogeosciences Laboratory (University of Burgundy,
237 Dijon, France). Oxygen isotope compositions have been corrected from the instrumental drift
238 and are reported in the standard delta notation relative to VPDB (Vienna PeeDee Belemnite)
239 in ‰ by assigning a $\delta^{18}\text{O}$ value of - 2.20 ‰ to NBS19. External reproducibility was better
240 that ± 0.08 ‰ (1 σ_{E}) for oxygen isotopes based that on multiple analyses of NBS19 along the
241 runs. Carbon isotopes (Suppl. Table 1) measured at the same time are also reported in the
242 delta notation relative to VPDB in ‰ by assigning a $\delta^{13}\text{C}$ value of + 1.95 ‰ to NBS19.
243 Carbon isotope reproducibility is better than ± 0.04 ‰ (1 σ_{E}).

244

245 3.3. *Clumped-isotope analyses*

246 Carbonate clumped-isotope thermometry is based on the quantification of statistical
247 anomalies in the abundance of doubly substituted isotopologues of carbonate groups (e.g.,
248 $^{13}\text{C}^{18}\text{O}^{16}\text{O}^{16}\text{O}^{2-}$). For thermodynamic reasons, the equilibrium abundance of ^{13}C – ^{18}O bonds in
249 a carbonate mineral increases as temperature decreases (e.g. Schauble et al., 2006), and this

250 isotopic signal may be preserved over geological time scales under favourable conditions
251 (Passey and Henkes, 2012; Stolper and Eiler, 2015). By precisely measuring the abundance of
252 the multiply-substituted, mass-47, isotopologues in the CO₂ produced by acid digestion of a
253 carbonate sample it is thus possible to constrain its original crystallization temperature
254 without making assumptions regarding the composition of parent waters (Ghosh et al., 2006;
255 Eiler et al., 2009).

256 Δ_{47} analyses generally require larger amounts of material than conventional, “single-
257 isotope” analyses, and their precision and accuracy are ultimately limited by ion counting
258 statistics and standardization issues. Each analysis reported here required from 2 to 3.5 mg,
259 and two or three replicate analyses per sample were performed (Table 2).

260 At Carry-Le-Rouet, nine of the larger shells already analyzed for $\delta^{18}\text{O}$ were selected
261 for Δ_{47} measurements. For the largest oyster (CAR17-6-33-b), two sub-sample carbonate
262 powders were collected separately from sections of the shell corresponding to minimum and
263 maximum $\delta^{18}\text{O}$ values, respectively. For the remaining shells, carbonate powder was collected
264 from the entire preserved oyster section (foliated calcite). At Castillon-Du-Gard, due to the
265 small size of the available bivalve fragments, each sample comprised carbonate from several
266 shell fragments collected from the same stratigraphic level or from adjacent stratigraphic
267 levels. Overall, samples were collected from 3 different stratigraphic levels, corresponding to
268 levels 9–12 m, 13–17 m, and 19.5–20.5 m.

269 The 13 clumped-isotope samples (considered of 2 or 3 aliquots each) were analyzed at
270 LSCE (Laboratoire des Sciences du Climat et de l'Environnement) using the equipment and
271 procedures described by Peral et al. (2018). Carbonate powders were dissolved in a common,
272 stirred, 104 % phosphoric acid bath at 90 °C for 15 minutes. After cryogenic removal of
273 water, the evolved CO₂ passed through a Porapak Q column (50/80 mesh, 1 m length, 2.1 mm
274 ID) held at –20 °C under helium 6.0 flow (25 mL/min). CO₂ was then quantitatively

275 recollected by cryogenic trapping, and transferred by gas expansion into an Isoprime 100
276 dual-inlet mass spectrometer equipped with six Faraday collectors (m/z 44 to 49). Each
277 analysis took about 3 hours, during which sample gas and working reference gas were
278 allowed to flow from matching, 10 mL reservoirs into the source, through a pair of fused
279 silica capillaries (65 cm length, 110 μm ID). Every 20 minutes, gas pressures were adjusted to
280 achieve a mass 44 current of 40 nA, with differences between sample and reference gas
281 generally below 0.1 nA. Background currents were measured in all high-gain collectors (m/z
282 45 to 49) before and after each pressure adjustment, with gas flowing into the source, and are
283 found to strongly correlate with the mass 44 current. Background-corrected ion current values
284 were processed using the IUPAC ^{17}O -correction parameters (Brand et al., 2010) to compute
285 $\delta^{13}\text{C}_{\text{VPDB}}$, $\delta^{18}\text{O}_{\text{VPDB}}$ and “raw” Δ_{47} values for each analysis. The isotopic composition ($\delta^{13}\text{C}$,
286 $\delta^{18}\text{O}$) of our working reference CO_2 was computed based on nominal $\delta^{13}\text{C}_{\text{VPDB}}$ and $\delta^{18}\text{O}_{\text{VPDB}}$
287 values for carbonate standard ETH-3 ($\delta^{13}\text{C}_{\text{VPDB}} = 1.71 \text{‰}$, $\delta^{18}\text{O}_{\text{VPDB}} = -1.78 \text{‰}$, Bernasconi et
288 al., 2018) and an oxygen-18 acid fractionation factor of 1.008176 (Das Sharma et al., 2002).
289 Three carbonate standards, ETH-1 to ETH-3 (Meckler et al., 2014; Bernasconi et al., 2018),
290 were then used to convert raw Δ_{47} to “absolute” Δ_{47} values, following the procedure described
291 by Daëron et al. (2016). The nominal Δ_{47} values for these standards are those recomputed by
292 Bernasconi et al. (2018) using IUPAC parameters: 0.258 ‰ for ETH-1, 0.256 ‰ for ETH-2
293 and 0.691 ‰ for ETH-3. The overall external reproducibility (standard deviation) of clumped
294 isotopes measurements for bivalve shells and standard is 14.6 ppm (n = 86).

295

296 *3.4. Strontium isotope analyses*

297 Twelve of the thirteen clumped-isotope samples were also analyzed for $^{87}\text{Sr}/^{86}\text{Sr}$
298 ratios. About 10 mg of carbonate powder were dissolved in a savillex beaker with 1 ml
299 solution of 2N HNO_3 on a hot plate at 70°C. The Sr was isolated from the matrix using

300 conventional Eichrom Sr-Spec columns. The strontium isotopic composition is measured
301 using a Thermo Triton Plus thermal ionization mass spectrometers at the GET laboratory
302 (Toulouse, France). The $^{87}\text{Sr}/^{86}\text{Sr}$ ratios were defined as the average of 150 measurements of
303 ion intensities following the static multi-collection mode normalized to $^{86}\text{Sr}/^{88}\text{Sr} = 0.1194$.
304 During the measurement period, the standard NBS 987 gave $^{87}\text{Sr}/^{86}\text{Sr}$ values of $0.710281 \pm$
305 0.000008 ($2 \sigma_D$, $n = 4$). The accuracy of our measurements is verified against the measured
306 ratios of international standards: 1) Jct-1 Giant Clam *Tridacna gigas* standard with a
307 measured value of 0.709175 ± 0.000010 ($2\sigma_D$; $n = 7$) and a certified value of $0.709150 \pm$
308 0.000050 (Ohno and Hirata, 2007); 2) CAL-S carbonate standard with a measured value of
309 0.706955 ± 0.000008 ($2 \sigma_D$; $n = 4$) and a certified value of 0.706924 ± 0.000018
310 (Yeghicheyan et al., 2014); and 3) IAPSO seawater standard with a measured value of
311 0.709181 ± 0.000003 ($2\sigma_D$; $n = 4$) and a certified value of 0.709179 ± 0.000005 (Nayar et al.,
312 2014). All $^{87}\text{Sr}/^{86}\text{Sr}$ ratios measured on our samples were adjusted to the NBS 987 standard
313 reference value of 0.710250.

314

315 **4. Results**

316 *4.1. Sedimentary study*

317 4.1.1. Carry-Le-Rouet outcrops

318 In the Carry-Le-Rouet section, the transitional continental to shallow marine
319 depositional environments develops following an E-W polarity. Four facies associations are
320 organized in four main depositional environments: (1) continental to coastal plain; (2) upper
321 shoreface; (3) restricted upper shoreface and (4) lower shoreface (Fig. 3A). Facies
322 descriptions are summarized in Table 1 and environmental interpretations are given below.

323

324 4.1.1.1. Continental to coastal plain environment

325 This environment groups facies A1 to A4 (Table 1). The presence of pedogenetic
326 horizons with rhizoliths, rare plant remains, mottling and carbonate nodules indicate
327 widespread subaerial, episodic sedimentation and soil formation. The marly deposits are
328 crosscut by sandy to conglomerate channels that correspond to sediment discharges in a
329 proximal alluvial plain (Miall, 1986). A1 is interpreted as a flood plain (Nury, 1990; Demory
330 et al., 2011). The clast-supported channels (Table 1; Fig. 3B1 and 3B2) and lobe-shape
331 conglomerates (A3 and A4) are interpreted as deltaic distributaries (Demory et al., 2011) or
332 alluvial fan delta (Nemec and Steel, 1988). The composition of the conglomerates indicates
333 several sources with a Nerthe (Barremian stage) carbonate origin for the monogenic ones and
334 Paleozoic basement (Permo-Triassic radiolarites or quartzites) for the polygenic conglomerates
335 (Demory et al., 2011). The presence of oysters encrusting the conglomerate boulders is
336 indicative of at least partly marine conditions during the deposition of the distal alluvial fan
337 system (Holmes, 1965), as oysters can be found in brackish or estuarine conditions.

338

339 4.1.1.2. Marine environment: Coastal plain to outer-platform

340 This environment encompasses facies B1 to D2 (Table 1). B1 consists of bioturbated
341 sandstones with cordon-rich conglomerates organized in planar stratifications. B1 is
342 interpreted as a coastal shallow marine environment in an upper shoreface (Table 1; Fig. 3B3
343 and 3B4; Nemec and Steel, 1988). The fine to coarse sandstones (B2) with megaripples,
344 Hummocky Cross-stratification (HCS) and convolute beds are interpreted as upper shoreface
345 zone (Table 1; Borgovini, 2003; Demory et al., 2011). Facies C consists of fine siltstone to
346 marls rich in mollusk (bivalves and gastropods), benthic and rare planktonic foraminifera as
347 *Globigerinoides trilobus*, *Globigerinoides altiaperturus* and *Catapsydrax dissimilis* and
348 echinoderms, corals and bryozoans. The absence of high-energy sedimentary structures, the
349 presence of marls to fine grain siltstones and the biotic association picture restricted marine

350 conditions in an upper shoreface environment (Table 1; Fig. 3B7 and 3B8). The carbonated
351 facies D1 is mainly composed of broken and disarticulated bioclats indicating intense
352 reworking and high-energy conditions in shoreface environment (Table 1; Nalin et al., 2010).
353 The D2 is composed of coral carpets and patches surrounded by bioclastic packstones (Table
354 1; Fig. 3B5 and 3B6; Riegl and Piller, 2000). The coral buildups and the bioclastic limestones
355 are interpreted as deposited in a shallow high-energy platform setting (Demory et al., 2011).

356

357 4.1.2. Castillon-Du-Gard outcrop

358 The sedimentology and stratigraphy of Middle Miocene succession of Castillon-Du-
359 Gard Sub-basin are revisited in Reynaud et al. (2012). In this study, the authors propose that
360 the succession of shallow cool-water carbonates (e.g. Castillon Molasse, Langhian-
361 Serravallian stages) alternates with offshore marls (e.g. Blue Marls, Burdigalian stage). Blue
362 Marls, close to the contact with the Vers unit are grainier and characterized by wave ripples in
363 sands and mollusk and foraminifera packstones (Molechfor; Reynaud et al., 2012). The biotic
364 components composed of molechfor and bryozoans and the wave ripples testify to proximal
365 offshore environment deposited in a low energy bay environment (Reynaud et al., 2012). Vers
366 unit (part of Castillon Molasse sub-unit) shows an erosional surface with the blue marls that
367 indicates decreasing accommodation space. This part of Castillon Molasse is a
368 packstone/rudstone with abundant bivalves and bryozoans (Bryomol; Reynaud et al., 2012).
369 This succession corresponds to shallow tidal deposits in a protected bay environment
370 (Reynaud et al., 2012). Castillon unit (part of Castillon Molasse sub-unit) is a floatstone
371 composed of bryozoan, mollusks and algae (Bryomol; Reynaud et al., 2012), interpreted as
372 subtidal dunes in a sand sheet deposited in deeper marine environments than the Vers Unit.
373 The top of this Castillon unit is a fine-grained packstone with bryozoans and mollusks

374 (Bryomol; Reynaud et al., 2012) infilling successive channels and is interpreted as a
375 decreasing water-depth with no emersion (Reynaud et al., 2012).

376

377 4.1.3. Age Model

378 The age model proposed for Carry-Le-Rouet is based on a biostratigraphic study
379 (Oudet et al., 2010) and a magnetostratigraphic one (Demory et al., 2011). Based on these two
380 dating methods, we propose ages for each stratigraphic level markers on Carry-Le-Rouet
381 section. Reefal unit (UR1 at 20 meters) is estimated at 23.03 Ma and marks the Chattian-
382 Aquitanian boundary. Reefal unit (UR2 at 25 meters; Fig. 3A) is dated at 22.9 Ma. Turritellid-
383 rich level (at 42 meters, Fig. 3) is dated at 22.27 Ma. Finally, two reefal units UR3 (at 61
384 meters; Fig. 3A) and UR4 (at 66 meters; Fig. 3A) are respectively dated at 21.01 Ma and
385 21.00 Ma. Tamaris unit has only been dated by biostratigraphy with an age of 18.10 Ma at the
386 base and 16.50 Ma at the top (Fondecave-Wallez et al., 1986). According to the literature, this
387 unit is overlaid by two Langhian bars (Anglada et al., 1988; Arnaud et al., 1988; Oudet et al.,
388 2010). An age of 15.97 Ma (Burdigalian-Langhian boundary) is proposed for the base of these
389 bars.

390 For Castillon-Du-Gard outcrop, transition between Uzès Molasse and Blue Marls
391 (base of the section) is dated at 15.97 Ma (Burdigalian-Langhian boundary). The Langhian-
392 Serravallian boundary (~ 13.82 Ma) is located within the Castillon Molasse (Reynaud et al.,
393 2012), despite limitation concerning available datation, we propose a position between 24 and
394 28 meters.

395

396 *4.2. Bivalve oxygen isotope composition*

397 Along the sedimentary succession at Carry-Le-Rouet, the bivalve $\delta^{18}\text{O}$ values display
398 relatively large scattering of about 4 ‰ within the same stratigraphic level (Fig. 4; Suppl.

399 Table 1). Similar scatter amplitudes are found within single oyster shells (e.g., level 21A).
400 Samples from the Chattian and Aquitanian stages yield $\delta^{18}\text{O}$ values ranging between about -4
401 and 0 ‰. By contrast, samples from the Burdigalian stage yield more positive $\delta^{18}\text{O}$ values
402 ranging between about -3 and 1 ‰. The youngest Late Burdigalian level yields more negative
403 $\delta^{18}\text{O}$ values than the rest of the Late Burdigalian stage.

404 Analyses performed on the largest oyster shells reveal different patterns of intra-shell
405 $\delta^{18}\text{O}$ variability. Two shells present a sinusoidal signal with an amplitude of $\delta^{18}\text{O}$ variations
406 up to ~ 4 ‰ (Fig. 5D and 5E). Two other shells present variations in $\delta^{18}\text{O}$ values with an
407 amplitude of about 3 ‰, that could recall a sinusoidal pattern with a truncation of the highest
408 $\delta^{18}\text{O}$ values (Fig. 5A and 5C). Two shells present a decrease in $\delta^{18}\text{O}$ values down to a plateau,
409 followed by an increase, with an amplitude of variation of 1 ‰ (Fig. 5F) and 3 ‰ (Fig. 5B).
410 A last shell presents more erratic variations in $\delta^{18}\text{O}$ values, within a ~ 1 ‰ range (Fig. 5G).
411 For hinges that were sampled with a high spatial resolution, we observe a decrease in the
412 amplitude of the signal between the Aquitanian (CAR17-6-28-a; CAR17-6-31base-a; CAR17-
413 6-33-b and CAR17-6-33-c) and the Burdigalian (CAR17-8-43-h and CAR17-8-43-i),
414 concomitantly with an overall increase in $\delta^{18}\text{O}$ values.

415 Similarly to the Carry-Le-Rouet section, $\delta^{18}\text{O}$ data from the Castillon-Du-Gard section
416 present a large dispersion (Fig. 4B), slightly higher than at Carry-Le-Rouet as it reaches about
417 5 ‰ in the Castillon Molasse (9 to 17 meters from the base of the section). $\delta^{18}\text{O}$ values seem
418 to increase at the top of the section, from average values of about -3.16 ‰ at about 20-22 m
419 from the base of the section to average $\delta^{18}\text{O}$ values around -1.57 ‰ at about 27-30 m from the
420 base of the section.

421

422 *4.3. Bivalve clumped isotope analyses*

423 The Δ_{47} values were measured on 12 bivalves and range between 0.676 and 0.716 ‰
424 (Table 2). They are not constant over time but fluctuate along the Carry-Le-Rouet and
425 Castillon-Du-Gard sections. The 5 analyzed Aquitanian samples present Δ_{47} values comprised
426 between 0.6852 ± 0.0093 ‰ and 0.705 ± 0.0095 ‰. One shell from the Aquitanian was large
427 enough to provide two subsamples (CAR17-6-33-b), one sampled in the part yielding
428 maximum $\delta^{18}\text{O}$ values from the microsampling approach, and the other in the part yielding
429 minimum $\delta^{18}\text{O}$ values (Fig. 5D). Both subsamples give quite close Δ_{47} values of $0.6821 \pm$
430 0.01 ‰ and 0.6823 ± 0.0099 ‰. The 3 analyzed Burdigalian samples yield lower values (p-
431 value of 0.08 based on a T-test), ranging from 0.6762 ± 0.0093 ‰ and 0.6882 ± 0.0093 ‰.
432 The 3 analyzed Langhian samples display the highest values of the studied interval, ranging
433 from 0.6968 ± 0.0098 ‰ and 0.7137 ± 0.0099 ‰ (higher than the Burdigalian samples : p-
434 value of 0.04 based on a T-test; and higher than the Aquitanian samples : p-value of 0.12
435 based on a T-test).

436

437 4.4. $^{87}\text{Sr}/^{86}\text{Sr}$ ratios

438 $^{87}\text{Sr}/^{86}\text{Sr}$ ratios range between 0.708222 and 0.708816 (Table 3). The strontium ratio
439 average for the Aquitanian is 0.708237, 0.708655 for the Late Burdigalian and 0.708830 for
440 Langhian stage. $^{87}\text{Sr}/^{86}\text{Sr}$ data increase about 600 ppm over the Aquitanian to Langhian time
441 period.

442

443 5. Discussion

444 5.1. Intra-shell variability of oyster clumped and oxygen isotope composition

445 Modern oysters and other bivalves often present growth cessation during part of the year,
446 when environmental conditions become stressful, due to extreme temperature, nutrient
447 availability, or seawater oxygenation (Brown and Hartwick, 1988; Mitchell et al., 2000; Surge

448 et al., 2001; Schöne 2008; Ulmann et al., 2013; Huygues et al., 2019) and can also occur
449 during reproduction (Clark et al., 1974, Paulet et al., 2006). The growth cessation can result in
450 an incomplete seasonal record of environmental parameters, namely temperature and seawater
451 $\delta^{18}\text{O}$ ($\delta^{18}\text{O}_{\text{sw}}$), archived in the carbonate $\delta^{18}\text{O}$ signal of the shells (Ullmann et al., 2010).
452 Growth cessation is apparent in shells CAR17-6-28-a and CAR17-6-31base-a (Fig. 5A and
453 5C), showing a truncated $\delta^{18}\text{O}$ signal at maximum $\delta^{18}\text{O}$ values. Therefore, only minimum
454 amplitude of seasonal variations in environmental parameters can be obtained in these shells,
455 along with temperature and $\delta^{18}\text{O}_{\text{sw}}$ during summer (represented by minimum carbonate $\delta^{18}\text{O}$
456 values, that are not truncated). We estimate that only 4 oysters may provide an estimation of
457 the full amplitude of seasonal temperature and $\delta^{18}\text{O}_{\text{sw}}$ variations (Fig. 5 B, D, E, F). Other
458 shells either present a truncated signal at maximum $\delta^{18}\text{O}$ values, or may not have lived long
459 enough to record a complete seasonal cycle. Alternatively, it cannot be excluded that some
460 shells (CAR17-8-43-I; Fig. 5G for instance) had a very low growth rate and that the sampling
461 resolution was not accurate enough to allow to identify the seasonal pattern.

462 We have first estimated temperature variations using the standard approach based on
463 carbonate $\delta^{18}\text{O}$ only, using the Anderson and Arthur (1983) equation established for calcitic
464 molluscs with the $\delta^{18}\text{O}_{\text{sw}}$ reconstructed by Billups and Schrag (2002), of -0.66 ‰ for the
465 Aquitanian, and of -0.94 ‰ for the Burdigalian. We have first considered a constant $\delta^{18}\text{O}_{\text{sw}}$
466 throughout the year to calculate the amplitude of seasonal temperature variations (ΔT) from
467 $\delta^{18}\text{O}$ values for the 4 largest micro-sampled oysters devoid of truncation in the $\delta^{18}\text{O}$ signal
468 (Fig. 5, B, D, E and F). The obtained ΔT with this approach range between 10 and 15°C for
469 the Aquitanian (Fig. 5, B, D and E) and around 5°C for the Late Burdigalian (Fig. 5, F). This
470 approach would thus show a ΔT decrease of 5 to 10°C between the Aquitanian and the Late
471 Burdigalian, along with a marked decrease in summer temperatures, of about 15°C. Pollen
472 assemblages indicate a temperate climate characterized by humid winters and drier summers

473 in Europe during the Late Burdigalian (Jiménez-Moreno et al., 2010; Bruch et al., 2011). Such
474 a climate would likely result in seasonal variations of local $\delta^{18}\text{O}_{\text{sw}}$ as well, with a higher
475 $\delta^{18}\text{O}_{\text{sw}}$ during summer and a lower $\delta^{18}\text{O}_{\text{sw}}$ during winter. Taking these suspected seasonal
476 variations of $\delta^{18}\text{O}_{\text{sw}}$ into consideration would lead to increased estimates of seasonal
477 temperature amplitude variations compared to those calculated using a constant $\delta^{18}\text{O}_{\text{sw}}$.

478 By comparison, the seasonal temperature contrast calculated from $\delta^{18}\text{O}$ variations
479 measured within Late Burdigalian oyster shells from Central Europe (Harzhauser et al., 2011),
480 also considering a constant $\delta^{18}\text{O}_{\text{sw}}$ throughout the year, is much higher ($\sim 10^\circ\text{C}$) as part of
481 another study. Summer temperatures calculated by these authors are also quite high at $\sim 28^\circ\text{C}$,
482 but close to the temperatures calculated from our Aquitanian oyster shells. Harzhauser et al.
483 (2011) report winter temperatures at $\sim 9\text{-}10^\circ\text{C}$ similar those obtained in this study for the Late
484 Burdigalian stage. This seasonal difference between the Aquitanian and the Late Burdigalian
485 may be explained by a microclimate on the Northwestern Mediterranean Sea margin during
486 the Late Burdigalian, or by different seasonal variations in salinity between the two regions,
487 as the oysters collected in Harzhauser et al. (2011) study come from estuarine environments
488 where the salinity is around 23 ‰. The Carry-Le-Rouet and Castillon-Du-Gard latitude
489 changed very little since the early Miocene at $\sim 43^\circ\text{N}$ (Jolivet et al., 2006). At present, the
490 annual water at ten meters water depth in the Gulf of Lion is around 18°C fluctuating between
491 winter temperatures of $13 \pm 1^\circ\text{C}$ and summer temperatures of $23 \pm 2^\circ\text{C}$ (Data from Levitus94;
492 Levitus and Boyer, 1994). This seasonal temperature variation of $\sim 10^\circ\text{C}$ is quite similar to our
493 estimates for the Aquitanian stage, although the temperatures calculated for this stage are
494 globally higher. By contrast, the Late Burdigalian seasonal contrast estimates are much
495 weaker compared to current one, with in addition cooler summer ($\sim 10^\circ\text{C}$) and winter ($\sim 15^\circ\text{C}$)
496 temperatures. This differs significantly from increasing temperatures recorded worldwide at

497 this period that marks the initiation of the climate warming leading to the MMCO during the
498 Langhian (Zachos et al., 2008; Jiménez-Moreno et al., 2010; Harzhauser et al., 2011).

499 An attempt was made to estimate seasonal seawater temperature contrast independently
500 from variations in $\delta^{18}\text{O}_{\text{sw}}$, based on clumped isotopes. Using conventional $\delta^{18}\text{O}$
501 measurements, complete seasonal cycles in temperature and $\delta^{18}\text{O}_{\text{sw}}$ may be identified in 4
502 oysters (Fig. 5 B, D, E and F) allowing to identify which part of the shells mineralized during
503 summer (minimum $\delta^{18}\text{O}$) versus winter (maximum $\delta^{18}\text{O}$), and these inferred seasonal extrema
504 were then sampled for Δ_{47} analyses. Unfortunately, due to the amount of material required per
505 Δ_{47} analysis and the small size of shells, only one Aquitanian shell (CAR17-6-33-b, Fig. 5D)
506 could be used, providing two sub-samples corresponding to the $\delta^{18}\text{O}$ minimum and maximum,
507 respectively (all other shells provided “bulk” shell material assumed to reflect weighted
508 average annual temperatures, and the corresponding results are presented in section 5.2.1).

509 There is today a large body of literature pertaining to the calibration of clumped-isotope
510 thermometry in biogenic and inorganic carbonates. Among other reasons, this is due to the
511 lingering methodological issues which have so far hindered precise inter-laboratory
512 comparisons (e.g., Petersen et al., 2019 and references therein). Here we opt for the recent
513 calibration by Peral et al. (2018), for two main reasons. For one thing, that study was
514 performed at LSCE using identical methods and instruments as those reported here. In
515 addition, despite the Peral et al. 2018 calibration being based on foraminifera, published and
516 unpublished results from LSCE yield a calibration function for modern oysters and pectens,
517 which is virtually identical to that of Peral et al. (2018).

518 The two “seasonal” sub-samples (CAR17-6-33-b-S1 and -W1) yield $\delta^{18}\text{O}$ values of -
519 3.6 ‰ and -1.3 ‰ respectively (Table 2), consistent with those obtained through
520 microsampling (Fig. 6, Areas 1-2). Somewhat surprisingly, the corresponding Δ_{47} -derived
521 temperatures (Fig. 6) are statistically indistinguishable (22.4 ± 3.1 °C versus 22.4 ± 3.1 °C, 1

522 σ_E). If these temperatures are used with the $\delta^{18}\text{O}$ values of the two shell subsamples and the
523 equation of Anderson and Arthur (1983), the resulting $\delta^{18}\text{O}_{\text{sw}}$ calculated are of -2.05 ‰ and
524 0.25 ‰ for the parts of the shell yielding minimum and maximum $\delta^{18}\text{O}$ values, respectively.
525 The absence of seasonal temperature variation appears unlikely considering the paleolatitude
526 of the Carry-Le-Rouet site during the Aquitanian (~10°C seasonality at this latitude at present
527 time), and considering independent estimates based on pollen data that point to the existence
528 of seasonal variations around 20°C in atmospheric temperature in Europe (Akgün et al.,
529 2007). This oyster shell yields the highest Δ_{47} -derived temperatures for the Aquitanian, 3°C
530 higher than the other analyzed shells (Table 2). As summer tend to be the period with the
531 highest growing rate in oysters from subtropical to temperate settings, it is possible that the
532 intra-shell $\delta^{18}\text{O}$ record defined with the microsampling method actually reflects a much
533 shorter time span of the oyster life than a year. The large variations in $\delta^{18}\text{O}$ recorded within
534 the oyster shell could then reflect punctual freshwater discharges within the same season. This
535 sample has been recovered from level 33, located at the transition between the Brackish
536 Rousset Unit and the Bioclastic Carry Unit (Demory et al., 2011). The presence of brackish
537 conditions in the lower part of the Bioclastic Carry Unit is supported by the presence of wood
538 fragments and reworked potamids, pointing to the existence of punctual freshwater discharges
539 in the shallow marine deposits of the Bioclastic Rousset unit.

540

541 *5.2. Miocene Climate Change in Mediterranean area*

542 5.2.1. Comparison between bivalve $\delta^{18}\text{O}$ values and benthic foraminifera $\delta^{18}\text{O}$

543 Bivalve $\delta^{18}\text{O}$ values present a large dispersion within each stratigraphic level, typically
544 around 4 ‰. As shown by the microsampling realized on sections of the largest oysters (Fig.
545 5) that presents one seasonality-cycle at most, most of the analyses performed on bivalve
546 fragments likely represent a relatively short time of the bivalve life, shorter than a year and

547 even maybe than a season. Thus, part of this large dispersion is likely to arise from seasonal
548 or intra-seasonal variations in temperature and $\delta^{18}\text{O}_{\text{sw}}$, as a bivalve fragment can have been
549 built mostly during a winter while another fragment recovered from the same stratigraphic
550 level may have formed mostly during summer. Due to this large dispersion, we applied a
551 statistical treatment to the dataset in order to identify significant climatic trends in the signal,
552 using the SiZer package (Sonderegger and Sonderegger, 2018) in the R software (R Core
553 Team 2017). The « SiZer » statistical method (based on studying statistical Significance of
554 ZERo crossings of smoothed estimates; Marron and Chaudhuri, 1998) has been widely used
555 on paleoclimatic proxies such as carbonate $\delta^{18}\text{O}$ values (increasing or decreasing) to detect
556 significant climatic trend at different timescales (Weckstrom et al., 2006; Dera et al., 2011;
557 Bougeault et al., 2017). This method is based on the construction of curves fitting time series
558 using different level of smoothing (h). The first derivatives of each curve are simultaneously
559 computed with their 95 % confidence intervals, allowing the signs of derivative estimated to
560 be statistically tested. If the sign of the first derivative is different from 0, including entire
561 95% confidence interval, then the corresponding trend shows a significant increase (for a
562 positive sign of the first derivative) or a significant decrease (for a negative sign of the first
563 derivative). These multiple tests are then represented as a map to identify the trend
564 significance for each size of smoothing. When the result is significant, it is coded in blue if it
565 is positive and in red if it is negative. On the contrary, it is coded in gray if it does not differ
566 from 0 and white when data are not numerous enough to identify significant trends ($n < 5$). A
567 Sizer map can thus be viewed as the summary of a large number (hundreds) of hypothesis test
568 results, with each pixel of the map representing the result of a hypothesis test where the null
569 hypothesis corresponds to the 0 slope. More formally, these tests are obtained from
570 confidence interval calculations using the row-wise method that is detailed in Hannig and
571 Marron (2006).

572 In this study, SiZer maps have been generated using a bandwidth h comprised between
573 0.1 and 10 Myrs (Fig. 7). This statistical treatment applied on carbonate $\delta^{18}\text{O}$ data highlights
574 the existence of a long-term increase in $\delta^{18}\text{O}$ values between 23 and 20 Ma followed by a
575 long-term decrease between 18 and 15 Ma. A second increase of $\delta^{18}\text{O}$ values is depicted as
576 well during the Serravallian, but over shorter timescales of about 1 to 2 Myrs. Using the
577 equation of Anderson and Arthur (1983) and a $\delta^{18}\text{O}_{\text{sw}}$ (Table 2) published by Billups and
578 Schrag (2002), as described in Section 5.1., these trends in $\delta^{18}\text{O}$ values depicted by the SiZer
579 map would correspond to (1) a cooling of about 10°C , from temperatures of about 25°C in the
580 Chattian and earliest Aquitanian to about 15°C in the Late Burdigalian, (2) a warming of
581 about 12°C , with temperatures up to 27°C on average during the Langhian, and (3) a shorter-
582 time cooling of about 4°C , with temperatures down to 23°C during the Serravallian (Fig. 8A).
583 Note that the $\delta^{18}\text{O}$ signal only depicts the cooling initiation that likely continues further into
584 the Serravallian.

585 Our new dataset recovered from shallow coastal environments presents some
586 similarities with the evolution of benthic foraminifera $\delta^{18}\text{O}$ ($\delta^{18}\text{O}_{\text{bf}}$; Zachos et al., 2008; Fig.
587 7). From the Chattian to the Burdigalian, the $\delta^{18}\text{O}$ increase highlighted by the SiZer map (Fig.
588 7) is coherent with the general increasing trend of $\delta^{18}\text{O}_{\text{bf}}$ values from the latest Oligocene to
589 the Burdigalian, although our dataset is not continuous enough to identify the shorter-time
590 Mi-events as evidenced in former studies (Zachos et al., 2008; Mawbey and Lear, 2014;
591 Beddow et al., 2016). The $\delta^{18}\text{O}$ minimum identified in our dataset during the Langhian could
592 well correspond to the MMCO (Zachos et al., 2008; Mawbey and Lear, 2013; Beddow et al.,
593 2016, Goldner et al., 2014; Holbourn et al., 2015; Super et al., 2018) detected in the $\delta^{18}\text{O}_{\text{bf}}$
594 dataset, while the $\delta^{18}\text{O}$ increase at the top the Castillon-Du-Gard succession could correspond
595 to the initiation of the MMCT (Zachos et al., 2001; Billups and Schrag, 2002; Shevenell et al.,
596 2004).

597 In contrast, the amplitude of the $\delta^{18}\text{O}$ variations is much larger in our bivalves
598 recovered from coastal environments compared to the deep marine environment record. The
599 Early Miocene cooling is expressed by an increase of 0.5 ‰ of the $\delta^{18}\text{O}_{\text{bf}}$ in deep marine
600 environment (Fig. 7) while the amplitude depicted by bivalve $\delta^{18}\text{O}$ at Carry-le-Rouet is four
601 times higher. Similarly, for the MMCO, the $\delta^{18}\text{O}_{\text{bf}}$ decreases by about 1 ‰ but about 2.5 ‰ in
602 our bivalve shells living in proximal environments. This amplitude difference is however
603 expected as shallow marine environments record larger temperature variations than deep-sea
604 environments during climate fluctuations. Both environments records variations in the ocean
605 $\delta^{18}\text{O}$ linked to the waning and waxing of polar ice-sheets. In shallow coastal environments, an
606 additional source of carbonate $\delta^{18}\text{O}$ variations is be related to the hydrological cycle, whose
607 variability in time and space can impact local $\delta^{18}\text{O}_{\text{sw}}$. Sedimentary facies at Carry-Le-Rouet
608 and Castillon-Du-Gard point to the persistence of an open marine depositional environment,
609 except for the Tamaris section which presents sedimentary facies coherent with a more
610 restricted bay environment (Fig. 3). Yet, even open marine environments are susceptible to be
611 impacted by nearby runoff leading to salinity variations, especially in coastal environments.
612 The sporadic occurrence of wood fragments and the low abundance of the fossils throughout
613 the Tamaris section may point to nearby freshwater inputs. Such an impact of local seawater
614 $\delta^{18}\text{O}$ fluctuations is further supported by the quite high temperatures of up to 35-40°C (Fig.
615 8A), calculated from bivalve $\delta^{18}\text{O}$ using the equation of Anderson and Arthur (1983) and the
616 $\delta^{18}\text{O}_{\text{sw}}$ of Billups and Schrag (2002) established for the global ocean, that most likely
617 exceeded the tolerance of bivalves (Stenzel, 1971). Thus, we anticipate that part of the large
618 variations recorded in the bivalve $\delta^{18}\text{O}$ signal may be related to change in the local
619 hydrological cycle in response to global climate change occurring at this period.

620

621 5.2.2. Evolution of shallow seawater temperatures inferred from clumped isotope analyses

622 “Bulk” Δ_{47} analyses, representing averaged isotopic composition over at least part of the
623 life span of the organisms (all shells except CAR17-6-33-b) could help decipher whether the
624 bivalve $\delta^{18}\text{O}$ signal is related to variations in seawater temperature and $\delta^{18}\text{O}_{\text{sw}}$. The Δ_{47} -
625 derived shallow seawater temperatures “ T_{47} ” (Table 2; Fig. 8A) range from $15.6 \pm 2.7^\circ\text{C}$ to
626 $22.4 \pm 3.1^\circ\text{C}$ ($1 \sigma_{\text{E}}$), with an average of $19.7 \pm 1.1^\circ\text{C}$ ($1 \sigma_{\text{E}}$, fully propagated from the
627 analytical errors on individual samples) which is cooler (p-value of 0.003 using a T-test) than
628 those calculated with the $\delta^{18}\text{O}_{\text{shell}}$ and a $\delta^{18}\text{O}_{\text{sw}}$ of Billups and Schrag (2002) for the
629 Aquitanian (about 25°C on average). Previous studies on pollen assemblages in Europe
630 (Akgün et al., 2007) and of coral assemblages in the Mediterranean Sea (Bosellini and Perrin,
631 2008), argue for atmospheric temperatures between 16.5 and 21.3°C and sea surface
632 temperatures between 18 and 19.3°C , respectively, during the Aquitanian stage. These values
633 are in good agreement with the temperatures calculated from our Δ_{47} analyses.

634 For the Late Burdigalian stage, shallow seawater T_{47} values are higher (Table 2; Fig. 8A)
635 than those for the Aquitanian (p-value of 0.048 using T-test), ranging between $20.5 \pm 2.8^\circ\text{C}$
636 and $24.3 \pm 2.9^\circ\text{C}$ ($1 \sigma_{\text{E}}$) and with an average of $22.6 \pm 1.7^\circ\text{C}$ ($1 \sigma_{\text{E}}$). These Late Burdigalian
637 temperatures calculated from Δ_{47} data are higher (p-value of 0.021 using a T-test) than those
638 calculated from bivalve $\delta^{18}\text{O}$ using a $\delta^{18}\text{O}_{\text{sw}}$ from Billups and Schrag (2002), by about 15°C
639 on average, but are again in better agreement with those published in the literature (Lecuyer et
640 al., 1996; Goedert et al., 2017). Indeed, with the exception of the slightly cooler temperatures
641 deduced from coral assemblages for the Late Burdigalian (18.5 to 20.5°C ; Bosellini and
642 Perrin, 2008), our temperature range is quite close to that deduced from combined analyses of
643 marine mammal and fish tooth $\delta^{18}\text{O}$, that is comprised between 20 and 28°C (Goedert et al.,
644 2017) in the northern Aquitaine Basin, and between 18 and 22°C in Brittany (Lecuyer et al.,
645 1996).

646 For the Langhian stage, T_{47} values range from $12.5 \pm 2.8^\circ\text{C}$ to $18 \pm 2.9^\circ\text{C}$ ($1 \sigma_E$) with an
647 average of $14.5 \pm 1.6^\circ\text{C}$ ($1 \sigma_E$). Again, these Langhian temperatures derived from Δ_{47} data are
648 cooler (p-value of 0.026 using a T-test), as for the Aquitanian (Table 2; Fig. 8A), than those
649 calculated from bivalve $\delta^{18}\text{O}$ using a $\delta^{18}\text{O}_{\text{sw}}$ from Billups and Schrag (2002), of about 25°C
650 on average. These values might appear cooler than expected, considering that this period
651 encompasses the MMCO for which both terrestrial and marine proxy data suggest globally
652 warmer conditions relative to the Early Miocene, especially at mid- and high latitudes
653 (Mosbrugger et al., 2005; Bruch et al., 2007; Bruch et al., 2011; Shevenell et al., 2008;
654 Zachos et al., 2008; Super et al., 2018). On the other hand, our clumped-isotope results are
655 coherent with atmospheric temperatures inferred from pollen assemblages on the
656 northwestern Mediterranean margin ($17\text{--}18^\circ\text{C}$, Bruch et al., 2007), and in Germany (16--
657 21°C , Böhme et al., 2007). Published sea surface temperatures inferred from combined $\delta^{18}\text{O}$
658 analyses of mammals and fish remains, are around $20^\circ\text{C} \pm 2^\circ\text{C}$ in Brittany (Lecuyer et al.,
659 1996), slightly higher than our Δ_{47} -derived temperatures. Additional estimates, calculated
660 from bivalve $\delta^{18}\text{O}$, range between 18 and 28°C in the Tethyan domain (Harzhauser et al.,
661 2011) and between 16.5 and 19.5°C from coral assemblage (Bosellini and Perrin, 2008).
662 Although the uncertainties associated with the calculation of all these temperatures are
663 difficult to estimate, they all tend to appear quite lower than the $27\text{--}37^\circ\text{C}$ range obtained from
664 TEX_{86} analyses at similar latitude in the central Atlantic (Super et al., 2018), similarly to our
665 Δ_{47} -derived temperature estimates. Our new temperature data inferred from Δ_{47} analyses are
666 thus coherent with the temperatures published in the literature for the Mediterranean and
667 Tethyan regions and support lower temperatures in this general area during the MMCO
668 compared to other sites at similar paleolatitude.

669 A relatively cool local to regional climate during the MMCO, compared to that inferred
670 from similar paleolatitudes based on TEX_{86} data, is also consistent with the high abundance of

671 bryozoans throughout the Castillon-Du-Gard section. The proliferation of bryozoans, mainly
672 in the form of encrusting cheilostomes, colonized the shallow seawater setting of the
673 Rhodano-Provencal Sub-basins and has been interpreted as deposited in temperate to warm
674 temperate depositional environment (Taylor and James, 2013). Similar bryozoan-rich deposits
675 in the Tethyan domain have been interpreted as cool-water carbonates by Randazzo et al.
676 (1999), based on $\delta^{18}\text{O}$ analyses and ecological reconstitutions. So far, such lower seawater
677 temperatures in the Mediterranean and Tethyan regions have been tentatively explained by the
678 deep cold-water arrivals coming from development of upwellings (Randazzo et al., 1999;
679 Reuter et al., 2013).

680 Thus the temperatures obtained from Δ_{47} analyses are in relatively good agreement
681 with those published in the literature in the general region, but quite markedly differ from
682 those obtained from bivalve $\delta^{18}\text{O}$ using the equation of Anderson and Arthur (1983) and the
683 $\delta^{18}\text{O}_{\text{sw}}$ of the global ocean of Billups and Schrag (2002). This apparent discrepancy between
684 Δ_{47} -derived and $\delta^{18}\text{O}$ -derived temperatures, observed for the different studied periods, can be
685 explained by modifications of the hydrological cycle linked to global climate change, leading
686 to a departure of the local $\delta^{18}\text{O}_{\text{sw}}$ from that of the global ocean estimated by Billups and
687 Schrag (2002).

688 5.2.3. Variations in the local hydrological cycle

689 In order to estimate the temporal evolution of the local $\delta^{18}\text{O}_{\text{sw}}$ we used the seawater
690 temperatures inferred from Δ_{47} analyses together with the $\delta^{18}\text{O}$ values of the oyster shells
691 measured on the same powder sample, and the Anderson and Arthur (1983) equation.

692 Our calculated values point to low local $\delta^{18}\text{O}_{\text{sw}}$ values during the Aquitanian (values
693 ranging from -3.9 to -1.06 ‰ with an average of -1.89 ‰), that are likely to reflect enhanced
694 precipitations and a lower salinity of the shallow neritic waters during this period (Table 2;
695 Fig. 8B). For the late Burdigalian, the calculated $\delta^{18}\text{O}_{\text{sw}}$ are much higher (p-value of 0,021

696 using a T-test), ranging from 0.9 to 1.71 ‰ with an average of 1.27 ‰, that points to a
697 decrease in precipitation and runoff and/or an increase in evaporation (Table 2; Fig. 8B). This
698 finding agrees well with the display of a low floro-faunal content in the Late Burdigalian of
699 the Tamaris succession, an absence of high-energy sedimentary structures and a deposition of
700 fine-grain sediments, suggesting that the depositional environment was potentially more
701 restricted. Our calculated $\delta^{18}\text{O}_{\text{sw}}$ values for the Late Burdigalian are close although slightly
702 lower than the estimation of about 2 ‰ on average for coastal seawater in the nearby
703 Aquitaine Basin during the Late Burdigalian by Goedert et al. (2017), based on combined
704 $\delta^{18}\text{O}$ analyses of marine mammals and fish remains. The local $\delta^{18}\text{O}_{\text{sw}}$ values for the Langhian
705 are again lower (ranging from -3.3 to -2.52 ‰, with on average of -3.02 ‰), which would
706 point to enhanced precipitations and runoff during this period (Table 2; Fig. 8B). These values
707 are significantly lower than those calculated for the Burdigalian (p-value of 0.0002 using a T-
708 test). The Castillon-Du-Gard Sub-basin is located on the periphery of the main Rhodano-
709 Provençal Basin, with the presence of nearshore facies (Bryomol) in the Castillon-Du-Gard
710 area (Reynaud et al., 2012), indicative of a semi-enclosed basin, and of sediments organized
711 in a regressive sequence. These conditions would further favor increased freshwater inputs
712 into this Sub-basin in the case of an enhanced hydrological cycle. In addition, a tectonically-
713 enhanced uplift of Alps chain occurred between the lower and the middle Miocene, that can
714 induce changes in the drainage pattern, major fluvial incisions, and increased runoff in the
715 Castillon-Du-Gard Sub-basin (Reynaud et al., 2012). In any case, following this coupled Δ_{47} -
716 $\delta^{18}\text{O}$ approach, our results would then point to the existence of changes in the local
717 hydrological cycle during the studied period, from the early to the middle Miocene.
718 Importantly, changes in local $\delta^{18}\text{O}_{\text{sw}}$, likely driven by changes in freshwater inputs, dominate
719 the recorded changes in bivalve $\delta^{18}\text{O}$, while temperature changes appear to have a more minor
720 influence (Fig. 9A and 9B).

721 Part of the local $\delta^{18}\text{O}_{\text{sw}}$ evolution reconstructed from the coupled Δ_{47} and $\delta^{18}\text{O}$
722 analyses in this study is due to changes in the ocean $\delta^{18}\text{O}_{\text{sw}}$ at a global scale, linked to
723 variations in ice-sheet volume on Antarctica at that time. In an attempt to estimate first-order
724 variations in local salinity due to changes in the local hydrological cycle only, we subtracted
725 to our calculated local $\delta^{18}\text{O}_{\text{sw}}$ the ocean $\delta^{18}\text{O}_{\text{sw}}$ (Fig. 8C) values published in Billups and
726 Schrag (2002), i.e. -0.66‰ VPDB (or -0.86‰ VSMOW ; see Grossmann (2012) for conversion
727 from the VPDB to the VSMOW scale) for the Aquitanian, -0.94‰ VPDB (or -1.14‰ VSMOW)
728 for the Burdigalian, and -0.71‰ VPDB (or -0.91‰ VSMOW) for the Langhian. We then used
729 salinity - $\delta^{18}\text{O}_{\text{sw}}$ relations established in modern environments but still comparable to the sites
730 investigated here. We chose for this rough approach the equation proposed by Railsback and
731 Anderson (1989) based on modern surface North Atlantic Ocean salinity and $\delta^{18}\text{O}_{\text{sw}}$ data. A
732 salinity - $\delta^{18}\text{O}_{\text{sw}}$ relation exists for the modern Mediterranean Sea (Pierre, 1999). However,
733 during the Miocene the Mediterranean Sea was still largely open to the Atlantic Ocean on the
734 west, and to the Indian Ocean on the east prior to its closure during the late Miocene (Jolivet
735 et al., 2006; Do Couto et al., 2016). Therefore, we think that this configuration of the
736 Mediterranean Sea during the Miocene, quite different than the modern one, likely impacted
737 the salinity - $\delta^{18}\text{O}_{\text{sw}}$ relation. To our opinion, it is thus preferable to consider the equation of
738 Railsback and Anderson (1989) based on surface North Atlantic data. Note that if the equation
739 of Pierre (1999) had been used instead, the estimated salinities presented below would be of
740 about 20 to 31‰ for the Aquitanian, about 40 to 43‰ for the Late Burdigalian and about 22
741 to 25‰ for the Langhian.

742 For the Aquitanian stage, the reconstructed salinities based on this approach tend to be
743 lower on average than the mean value of 35‰ of the modern open ocean, with an important
744 variability in the 30 and 34‰ range based on bulk shells, i.e an average salinity throughout
745 the bivalve life (Table 2; Fig. 8D). This points to a contribution of freshwater inputs to the

746 local seawater by runoff, rainfall, or groundwater discharge, although this range remains
747 within the tolerance of the stenohalin organisms (corals, bryozoans, echinoids and
748 foraminifera) observed at Carry le Rouet during the Aquitanian (Oertli, 1964). The Sr isotope
749 composition of bivalve shells can provide additional insights on potential freshwater inputs, if
750 they are large enough to impact the local seawater Sr budget. The strontium isotope
751 composition ($^{87}\text{Sr}/^{86}\text{Sr}$) of bio-carbonates reflects the isotopic composition of the water in
752 which they form their test (Veizer et al., 1999; Palmer and Elderfield, 1985). Therefore, the
753 $^{87}\text{Sr}/^{86}\text{Sr}$ ratios measured on carbonated organisms enable to reconstruct the isotopic signature
754 of the aqueous environment in which they thrive.

755 The measured $^{87}\text{Sr}/^{86}\text{Sr}$ of the bivalves compares well with the Sr isotope signatures of
756 planktonic foraminifera and of mixed calcitic fossils from the Umbria-March Basin (Fig. 8E;
757 Kocsis et al., 2008; Cornacchia et al., 2018). Our Sr isotope record mostly falls within the
758 global seawater Sr isotope reference curve (McArthur and Howarth, 2004), when considering
759 a seawater $^{87}\text{Sr}/^{86}\text{Sr}$ variability comparable to that recorded in the modern ocean (± 50 ppm;
760 El Meknassi et al., 2018). For the Aquitanian, the $^{87}\text{Sr}/^{86}\text{Sr}$ of our samples tends to fall at the
761 lower limit of this range, and even presents slightly more unradiogenic values than that of the
762 open ocean at that time, as observed from the nearby Umbria-March Basin (Kocsis et al,
763 2008; Fig. 8E). This slight deviation from the open ocean Sr isotope composition may derive
764 from active volcanism in the region, that can release mantle-derived unradiogenic Sr signature
765 into the local seawater and influence its Sr budget. Sporadic volcanic activity during the
766 Miocene in the western Mediterranean Sea can indeed be generated during the extension of
767 the Tyrrhenan and Algéro-Provencal basins (Frizon de Lamotte et al., 2000; Schettino and
768 Turco, 2011; Bialik et al., 2019). Large eruptions within the 25-19 Ma interval are supported
769 by volcanoclastic sediments in the vicinity of the studied region (from Provence to Sardinia
770 and Corsica and in the Umbria-March Basin ; Montanari et al., 1994; Beccaluva et al., 2004),

771 and by radiogenic ϵ_{Nd} and unradiogenic $^{87}Sr/^{86}Sr$ values of sediments from the Umbria-March
772 region (Kocsis et al., 2008).

773 Alternatively, it has been shown that large riverine inputs can also result in a deviation of
774 the Sr isotope composition of neritic seawater from that of the global ocean (Bryant et al.,
775 1995; El Meknassi et al., 2018). At Carry-le Rouet, the Miocene deposits unconformably rest
776 on marine carbonates from the Lower Cretaceous (Barremian to Lower Aptian), that are
777 characterized by low $^{87}Sr/^{86}Sr$ values (typically within the 0.7073 to 0.70745 range; McArthur
778 and Howarth, 2004). Enhanced freshwater input should then result in a decrease of local
779 seawater $^{87}Sr/^{86}Sr$, if large enough to impact the local Sr budget. Bryant et al. (1995) has
780 shown that a measurable effect occurs at salinities below 12 ‰. Salinities calculated from our
781 coupled $\delta^{18}O-\Delta_{47}$ approach lay however in the 30 to 34 ‰ range for this interval at Carry-le-
782 Rouet, and the impact of freshwater inputs on the local seawater Sr isotope composition
783 should then have remained limited. Yet recent studies reported that deviation from the global
784 ocean $^{87}Sr/^{86}Sr$ value can occur at higher salinities, above 30 ‰ (Huang et al., 2011),
785 especially in environments affected by submarine groundwater discharges that can have
786 elevated Sr concentrations when deriving from carbonate-rock aquifer systems (Trezzi et al.,
787 2017; El Meknassi et al., 2018). Thus enhanced riverine inputs may also have contributed to
788 lower the $^{87}Sr/^{86}Sr$ value of the local seawater at Carry-le-Rouet.

789 Conversely, for the Late Burdigalian, the reconstructed salinities are much higher (p-
790 value of 0.0014 using a T-test), in the 38 to 39 ‰ range (Table 2; Fig. 8D). This would
791 correspond to a hypersaline environment with reduced runoff and high evaporation, in
792 agreement with the higher temperatures inferred from our Δ_{47} analyzes in the Late Burdigalian
793 compared to the Aquitanian. Such high salinities are consistent with the disappearance of
794 stenohalin organisms and the restricted environmental conditions recorded at the Tamaris
795 section. High evaporation should not affect $^{87}Sr/^{86}Sr$ values of seawater, which is coherent

796 with the $^{87}\text{Sr}/^{86}\text{Sr}$ values recorded by our bivalves, mostly within the expected range of
797 signature for the open ocean at that time.

798 The calculated salinities for the Langhian stage lay between 30 and 32 ‰ (Table 2;
799 Fig. 8D), significantly lower than those calculated for the Burdigalian (p-value of 0.00002,
800 using a T-test). Combined with the quite cool temperatures deduced from Δ_{47} for this period,
801 this suggests again a marine environment subjected to freshwater inputs. A cooler and slightly
802 brackish environment during the MMCO at Castillon-Du-Gard would agree with the
803 proliferation of bryozoans and associated algae in these levels. Similar facies association is
804 described in middle Miocene marine sediments from Austria and considered as deposited in a
805 temperate environment with low salinity (Friebe, 1994). Modern bryozoan ecological
806 reconstructions, occupy a wide variety of environments and can tolerate salinities ranging
807 from 32 to 37 ‰ (Ryland, 1970; Smith, 1995) and temperatures from 10 to 30°C (Domack,
808 1988), that are within the temperature and salinity ranges inferred from our coupled $\Delta_{47} - \delta^{18}\text{O}$
809 approach at Castillon-Du-Gard.

810 The Sr isotope composition of Langhian bivalves from the Castillon-du-Gard section fall
811 within the Sr isotope reference curve for the open ocean at that time (Fig. 8E), although our
812 coupled $\delta^{18}\text{O} - \Delta_{47}$ approach points to salinities comparable to that obtained for the Aquitanian.
813 Deviations toward more radiogenic values at that time were reported from mixed fossils from
814 sites closer to the Alps, as exposure of older continental rocks contributes to imprint river
815 waters with a radiogenic Sr isotope composition (Kocsis et al., 2008; 2009). Surface runoff
816 issued from watersheds in Western Europe exhibits at present quite radiogenic Sr isotope
817 signature (of 0,7093 on average ; Peucker-Ehrenbrink and Fiske, 2019). The Castillon-du-
818 Gard section, located north to the Carry-le-Rouet section within a narrow and incised valley,
819 could have received a larger contribution from river waters draining the Alps watersheds,
820 especially in the context of the tectonically-enhanced uplift of the Alps during the Miocene

821 (Frisch et al., 2000; Reynaud et al., 2012). Rivers draining old continental material tend to
822 yield much lower Sr concentrations than rivers or groundwaters draining carbonate
823 lithologies. It is thus possible that the enhanced freshwater inputs during the MMCO, inferred
824 from the salinities calculated from the $\delta^{18}\text{O}$ and Δ_{47} values, were not large enough at
825 Castillon-du-Gard to significantly shift the local seawater $^{87}\text{Sr}/^{86}\text{Sr}$ ratio.

826

827 **6. Conclusions**

828 Our multi-proxy approach based on both $\delta^{18}\text{O}$ and Δ_{47} analyses of bivalves recovered
829 from two outcrops in southern France during the Miocene highlight a warming ($\sim 3^\circ\text{C}$) of the
830 North-West Mediterranean coastal marine environments between the Aquitanian and the Late
831 Burdigalian, accompanied by an increase in local salinity probably linked to more restricted
832 conditions. Surprisingly, low $\delta^{18}\text{O}$ values recorded in the Langhian, supposedly during the
833 MMCO, are associated with cooler seawater temperatures (between $13 - 18^\circ\text{C}$) inferred from
834 Δ_{47} analyzes. This apparent discrepancy can be reconciled if a modification occurred in the
835 local hydrological cycle linked to the overall warmer conditions recorded at a global scale
836 during this event, leading to enhanced discharges of freshwaters in the region during the
837 MMCO. The existence of relatively cool and low salinity local waters would be consistent is
838 with the development of an abundant bryozoan fauna observed at that time in the studied
839 section. Local freshwater discharges at the regional scale could also have been promoted by
840 change in the pattern of the drainage system driven by local tectonic uplift and a narrowing of
841 the corridor structure of the Rhodano-Provencal. The Sr isotope analyses performed on the
842 bivalves from the two studied sections are compatible with the existence of freshwater inputs
843 during the Aquitanian and the Langhian in this region. These inputs were however not large
844 enough to result in large deviations of the local seawater $^{87}\text{Sr}/^{86}\text{Sr}$ composition from that of
845 the global ocean, which is consistent with the reconstructed salinities, laying in the 30-34 ‰

846 range. Importantly, our results illustrate the risks inherent to paleotemperature reconstructions
847 based solely on $\delta^{18}\text{O}$ records and highlight the pertinence of coupling several
848 paleoenvironmental and paleoclimatic proxies, geochemical ($\delta^{18}\text{O} - \Delta_{47}$) or sedimentological,
849 to reconstruct the variations of seawater temperature and salinity in shallow coastal
850 environments. The combined $\delta^{18}\text{O} - \Delta_{47}$ approach thus appears promising to study the local
851 response to global climatic variations in environments that are subjected to salinity variations
852 (lagoonal, mangrove or estuarine environments). Understanding how such environments react
853 to climate change would help to better constrain the behavior of our climate system. Our work
854 highlights the importance of a continuous effort in gathering new data from different regions
855 of the world during MMCO, to capture the diversity of local responses to a global climatic
856 change.

857

858

859

Acknowledgements

860 We wish to thank T. COCQUEREZ (Biogeosciences Laboratory, University of Burgundy) for
861 the isotopic analyses. We wish also to thank F. MONNA and R. LAFFONT (Biogeosciences
862 Laboratory, University of Burgundy) for help with statistical treatment of our data. This study
863 was funded by the ANR AMOR, coordinated by Y. DONNADIEU.

864

865

References

866 Akgün, F., Kayseri, M. S., and Akkiraz, M. S. 2007. Palaeoclimatic evolution and
867 vegetational changes during the Late Oligocene–Miocene period in Western and
868 Central Anatolia (Turkey). *Palaeogeography, Palaeoclimatology, Palaeoecology*,
869 253(1), 56-90. <https://doi.org/10.1016/j.palaeo.2007.03.034>.

870 Al-Aasm, I. S., and Veizer, J. 1986. Diagenetic stabilization of aragonite and low-Mg calcite;
871 I, Trace elements in rudists. *Journal of Sedimentary Research*, 56(1), 138-152.
872 <https://doi.org/10.1306/212F88A5-2B24-11D7-8648000102C1865D>.

873 Anglada, R., Gourinard, Y., Lesueur, J. L., and Rubino, J.-L., 1988. Les séquences de dépôt
874 du Burdigalien et du Langhien de Basse Provence (Littoral de la Nerthe et région des
875 Etangs). *Livret Guide d'Excursion Coll. « Paléobathymétrie, eustatisme et séquence
876 de dépôts »*, Marseille, juin 1988: 34p.

877 Anderson, T. F., and Arthur, M. A. 1983. Stable isotopes of oxygen and carbon and their
878 application to sedimentologic and paleoenvironmental problems. *Unknown Journal*.

879 Andreieff, P., Anglada, R., Carbonnel, G., Catzigras, F., Cavelier, C., Chateauneuf, J. J.,
880 Colomb, E., Jacob, C., Lai, J., l'Hommer., A., Lezaud, L., Lorenz, C., Mercier, H., and
881 Parfenoff, A. 1972. Contribution à l'étude de Carry-le-Rouet (Bouches-du-Rhône).
882 Cinquième congrès du Néogène Méditerranéen, *Mémoire du BRGM*, 3, 132.

883 Arnaud, M., Barbaroux, L., Catzigras, F., Colomb, E., Monleau, C., 1988. Le Burdigalien et
884 la Langhien de Provence occidentale (Bouches-du-Rhône): nouvelles données
885 stratigraphiques et sédimentologiques. *Comptes Rendus de l'Académie des Sciences*
886 307(II): 779-784.

887 Beccaluva, L., Coltorti, M., Giunta, G., and Siena, F. 2004. Tethyan vs. Cordilleran
888 ophiolites: a reappraisal of distinctive tectono-magmatic features of supra-subduction
889 complexes in relation to the subduction mode. *Tectonophysics*, 393(1-4), 163-174.
890 <https://doi.org/10.1016/j.tecto.2004.07.034>.

891 Beddow, H. M., Liebrand, D., Sluijs, A., Wade, B. S., and Lourens, L. J. 2016. Global change
892 across the Oligocene-Miocene transition: High-resolution stable isotope records from
893 IODP Site U1334 (equatorial Pacific Ocean). *Paleoceanography*, 31(1), 81-97.
894 <https://doi.org/10.1002/2015PA002820>.

- 895 Bernasconi, S. M., Müller, I. A., Bergmann, K. D., Breitenbach, S. F., Fernandez, A., Hodell,
896 D. A., Jaggi, M., Nele-Meckler, A., Millan, I., and Ziegler, M. 2018. Reducing
897 uncertainties in carbonate clumped isotope analysis through consistent carbonate-
898 based standardization. *Geochemistry, Geophysics, Geosystems*, 19(9), 2895-2914.
899 <https://doi.org/10.1029/2017GC007385>.
- 900 Bialik, O. M., Frank, M., Betzler, C., Zammit, R., and Waldmann, N. D. 2019. Two-step
901 closure of the Miocene Indian Ocean Gateway to the Mediterranean. *Scientific*
902 *Reports*, 9(1), 8842.<https://doi.org/10.1038/s41598-019-45308-7>.
- 903 Billups, K., and Schrag, D. P. 2002. Paleotemperatures and ice volume of the past 27 Myr
904 revisited with paired Mg/Ca and $^{18}\text{O}/^{16}\text{O}$ measurements on benthic foraminifera.
905 *Paleoceanography*, 17(1), 3-1. <https://doi.org/10.1029/2000PA000567>.
- 906 Böhme, M., Bruch, A. A., and Selmeier, A. 2007. The reconstruction of Early and Middle
907 Miocene climate and vegetation in Southern Germany as determined from the fossil
908 wood flora. *Palaeogeography, Palaeoclimatology, Palaeoecology*, 253(1), 91-114.
909 <https://doi.org/10.1016/j.palaeo.2007.03.035>.
- 910 Borgovini, R. 2003. Stratigraphie et facies de la base du cycle Néogène de Basse Provence
911 (littoral de la Nerthe : Carry-Le-Rouet, Sausset-Les-Pins). Rapport Total, Exploration
912 and Production, DGEP/GSR/TG/THEM N°03-006 : 134.
- 913 Bosellini, F. R., and Perrin, C. 2008. Estimating Mediterranean Oligocene–Miocene sea-
914 surface temperatures: an approach based on coral taxonomic richness.
915 *Palaeogeography, Palaeoclimatology, Palaeoecology*, 258(1-2), 71-88.
916 <https://doi.org/10.1016/j.palaeo.2007.10.028>.
- 917 Bougeault, C., Pellenard, P., Deconinck, J. F., Hesselbo, S. P., Dommergues, J. L., Bruneau,
918 L., Cocquerez, T., Laffont, R., Huret, A., and Thibault, N. 2017. Climatic and
919 palaeoceanographic changes during the Pliensbachian (Early Jurassic) inferred from

920 clay mineralogy and stable isotope (CO) geochemistry (NW Europe). *Global and*
921 *Planetary Change*, 149, 139-152. <https://doi.org/10.1016/j.gloplacha.2017.01.005>.

922 Bougeois, L., De Raféllis, M., Reichart, G. J., De Nooijer, L. J., Nicollin, F., and Dupont-
923 Nivet, G. 2014. A high resolution study of trace elements and stable isotopes in oyster
924 shells to estimate Central Asian Middle Eocene seasonality. *Chemical Geology*, 363,
925 200-212. <https://doi.org/10.1016/j.chemgeo.2013.10.037>.

926 Bougeois, L., De Raféllis, M., Reichart, G. J., de Nooijer, L. J., and Dupont-Nivet, G. 2016.
927 Mg/Ca in fossil oyster shells as palaeotemperature proxy, an example from the
928 Palaeogene of Central Asia. *Palaeogeography, Palaeoclimatology, Palaeoecology*, 441,
929 611-626. <https://doi.org/10.1016/j.palaeo.2015.09.052>.

930 Brand, U., and Veizer, J. 1981. Chemical diagenesis of a multicomponent carbonate system;
931 2, Stable isotopes. *Journal of Sedimentary Research*, 51(3), 987-997.
932 <https://doi.org/10.1306/212F7DF6-2B24-11D7-8648000102C1865D>.

933 Brand, W. A., Assonov, S. S., and Coplen, T. B. 2010. Correction for the ¹⁷O interference in δ
934 (¹³C) measurements when analyzing CO₂ with stable isotope mass spectrometry
935 (IUPAC Technical Report). *Pure and Applied Chemistry*, 82(8), 1719-1733.
936 <https://doi.org/10.1351/PAC-REP-09-01-05>.

937 Brown, J. R., and Hartwick, E. B. 1988. Influences of temperature, salinity and available food
938 upon suspended culture of the Pacific oyster, *Crassostrea gigas*: I. Absolute and
939 allometric growth. *Aquaculture*, 70(3), 231-251. [https://doi.org/10.1016/0044-](https://doi.org/10.1016/0044-8486(88)90099-3)
940 [8486\(88\)90099-3](https://doi.org/10.1016/0044-8486(88)90099-3).

941 Bruch, A. A., Utescher, T., Olivares, C. A., Dolakova, N., Ivanov, D., and Mosbrugger, V.
942 2004. Middle and Late Miocene spatial temperature patterns and gradients in Europe-
943 preliminary results based on palaeobotanical climate reconstructions. *Courier-*
944 *Forschungsinstitut Senckenberg*, 15-28.

- 945 Bruch, A. A., Uhl, D., and Mosbrugger, V. 2007. Miocene climate in Europe—patterns and
946 evolution: a first synthesis of NECLIME. *Palaeogeography, Palaeoclimatology,*
947 *Palaeoecology*, 253(1-2), 1-7. <https://doi.org/10.1016/j.palaeo.2007.03.030>.
- 948 Bruch, A. A., Utescher, T., and Mosbrugger, V. 2011. Precipitation patterns in the Miocene of
949 Central Europe and the development of continentality. *Palaeogeography,*
950 *Palaeoclimatology,* *Palaeoecology*, 304(3-4), 202-211.
951 <https://doi.org/10.1016/j.palaeo.2010.10.002>.
- 952 Bryant, J. D., Jones, D. S., and Mueller, P. A. 1995. Influence of freshwater flux on $^{87}\text{Sr}/^{86}\text{Sr}$
953 Sr chronostratigraphy in marginal marine environments and dating of vertebrate and
954 invertebrate faunas. *Journal of Paleontology*, 69(1), 1-6.
955 <https://doi.org/10.1017/S002233600002686X>.
- 956 Choquette, P. W., and James, N. P. 1990. Limestones—the burial diagenetic environment.
957 *Diagenesis: Geoscience Canada, Reprint Series*, 4, 75-111.
- 958 Clark Jr, R. C., Finley, J. S., and Gibson, G. G. 1974. Acute effects of outboard motor effluent
959 on two marine shellfish. *Environmental Science and Technology*, 8(12), 1009-1014.
- 960 Cornacchia, I., Agostini, S., and Brandano, M. 2018. Miocene Oceanographic Evolution
961 Based on the Sr and Nd Isotope Record of the Central Mediterranean.
962 *Paleoceanography and Paleoclimatology*, 33(1), 31-47.
963 <https://doi.org/10.1002/2017PA003198>.
- 964 Cramwinckel, M. J., Huber, M., Kocken, I. J., Agnini, C., Bijl, P. K., Bohaty, S. M., Frieling,
965 J., Goldner, A., Hilgen, F. J., Kip, E. L., Peterse, F., Van Der Ploeg, R., Röhl, U.,
966 Schouten, S., Sluijs, A. 2018. Synchronous tropical and polar temperature evolution in
967 the Eocene. *Nature*, 559(7714), 382. <https://doi.org/10.1038/s41586-018-0272-2>.

968 Daëron, M., Blamart, D., Peral, M., and Affek, H. P. 2016. Absolute isotopic abundance ratios
969 and the accuracy of Δ_{47} measurements. *Chemical Geology*, 442, 83-96.
970 <https://doi.org/10.1016/j.chemgeo.2016.08.014>.

971 Das Sharma, S., Patil, D. J., and Gopalan, K. 2002. Temperature dependence of oxygen
972 isotope fractionation of CO₂ from magnesite-phosphoric acid reaction. *Geochimica et*
973 *Cosmochimica Acta*, 66(4), 589-593. [https://doi.org/10.1016/S0016-7037\(01\)00833-](https://doi.org/10.1016/S0016-7037(01)00833-)
974 X.

975 Demarcq, G. 1970. Étude stratigraphique du Miocène rhodanien. *Mém. BRGM*, n°61, 257 p.

976 Demory, F., Conesa, G., Oudet, J., Mansouri, H., Münch, P., Borgomano, J., Thouveny, N.,
977 Lamarche, J., Gisquet, F., and Marié, L. 2011. Magnetostratigraphy and
978 paleoenvironments in shallow-water carbonates: the Oligocene-Miocene sediments of
979 the northern margin of the Liguro-Provençal basin (West Marseille, southeastern
980 France). *Bulletin de la Société géologique de France*, 182(1), 37-55.
981 <https://doi.org/10.2113/gssgfbull.182.1.37>.

982 Dera, G., Brigaud, B., Monna, F., Laffont, R., Pucéat, E., Deconinck, J. F., Pellenard, P.,
983 Joachimski, M. M., and Durlet, C. 2011. Climatic ups and downs in a disturbed
984 Jurassic world. *Geology*, 39(3), 215-218. <https://doi.org/10.1130/G31579.1>.

985 Diester-Haass, L., Billups, K., Gröcke, D. R., François, L., Lefebvre, V., and Emeis, K. C.
986 2009. Mid-Miocene paleoproductivity in the Atlantic Ocean and implications for the
987 global carbon cycle. *Paleoceanography and Paleoclimatology*, 24(1).
988 <https://doi.org/10.1029/2008PA001605>.

989 Do Couto, D., Gorini, C., Jolivet, L., Lebret, N., Augier, R., Gumiaux, C., d'Acremont, E.,
990 Ammar, A., Jabour, H., and Auxietre, J. L. 2016. Tectonic and stratigraphic evolution
991 of the Western Alboran Sea Basin in the last 25 Myrs. *Tectonophysics*, 677, 280-311.
992 <https://doi.org/10.1016/j.tecto.2016.03.020>.

- 993 Domack, E. W. 1988. Biogenic facies in the Antarctic glacial marine environment: basis for a
994 polar glacial marine summary. *Palaeogeography, Palaeoclimatology, Palaeoecology*,
995 63(4), 357-372. [https://doi.org/10.1016/0031-0182\(88\)90105-8](https://doi.org/10.1016/0031-0182(88)90105-8).
- 996 Eiler, J. M., Bonifacie, M., and Daëron, M. 2009. 'Clumped isotope' thermometry for high-
997 temperature problems. *Geochimica et Cosmochimica Acta*, 73(13), A322-A322.
998 <http://dx.doi.org/10.1016/j.gca.2009.05.004>.
- 999 El Meknassi, S., Dera, G., Cardone, T., De Rafélis, M., Brahmi, C., and Chavagnac, V. 2018.
1000 Sr isotope ratios of modern carbonate shells: Good and bad news for
1001 chemostratigraphy. *Geology*, 46(11), 1003-1006. <https://doi.org/10.1130/G45380.1>.
- 1002 Faccenna, C., Mattei, M., Funiciello, R., and Jolivet, L. 1997. Styles of back-arc extension in
1003 the central Mediterranean. *Terra Nova*, 9(3), 126-130. <https://doi.org/10.1046/j.1365-3121.1997.d01-12.x>.
- 1005 Ferrandini, M., BouDagher-Fadel, M. K., Ferrandini, J., Oudet, J., and André, J. P. 2010.
1006 Nouvelles observations sur les Miogypsinidés du Miocène inférieur et moyen de
1007 Provence et de Corse (France) et de Sardaigne septentrionale (Italie). In *Annales de*
1008 *Paléontologie*. Vol. 96, No. 3, pp. 67-94. <https://doi.org/10.1016/j.annpal.2011.04.002>.
- 1009 Foster, G. L., Lear, C. H., and Rae, J. W. 2012. The evolution of pCO₂, ice volume and
1010 climate during the middle Miocene. *Earth and Planetary Science Letters*, 341, 243-
1011 254. <https://doi.org/10.1016/j.epsl.2012.06.007>.
- 1012 Fondecave-Wallez, M. J., Magné, J., Gourinard, Y., and Demarcq, G. 1986. Nouvelles grade-
1013 datations de sédiments burdigaliens des régions rhodaniennes. *Géologie*
1014 *Méditerranéenne*, 12(1), 59-63. <https://doi.org/10.3406/geolm.1985.1339>.
- 1015 Friebe, J. G. 1994. Serpulid-bryozoan-foraminiferal biostromes controlled by temperate
1016 climate and reduced salinity: Middle Miocene of the Styrian Basin, Austria. *Facies*,
1017 30(1), 51-62. <https://doi.org/10.1007/BF02536889>.

1018 Frisch, W., Dunkl, I., & Kuhlemann, J. 2000. Post-collisional orogen-parallel large-scale
1019 extension in the Eastern Alps. *Tectonophysics*, 327(3-4), 239-265.
1020 [https://doi.org/10.1016/S0040-1951\(00\)00204-3](https://doi.org/10.1016/S0040-1951(00)00204-3).

1021 Frizon de Lamotte, D., Saint Bezar, B., Bracène, R., and Mercier, E. 2000. The two main
1022 steps of the Atlas building and geodynamics of the western Mediterranean. *Tectonics*,
1023 19(4), 740-761. <https://doi.org/10.1029/2000TC900003>.

1024 Galeotti, S., DeConto, R., Naish, T., Stocchi, P., Florindo, F., Pagani, M., Barrett, P., Bohaty,
1025 S. M., Lanci, L. Pollard, D., Sandroni, S., Talarico, F. M., Zachos, J. C. 2016.
1026 Antarctic Ice Sheet variability across the Eocene-Oligocene boundary climate
1027 transition. *Science*, 352(6281), 76-80. <https://doi.org/10.1126/science.aab0669>.

1028 Gasson, E., DeConto, R. M., Pollard, D., and Levy, R. H. 2016. Dynamic Antarctic ice sheet
1029 during the early to mid-Miocene. *Proceedings of the National Academy of Sciences*,
1030 113(13), 3459-3464. <https://doi.org/10.1073/pnas.1516130113>.

1031 Gattacceca, J., Deino, A., Rizzo, R., Jones, D. S., Henry, B., Beaudoin, B., and Vadeboin, F.
1032 2007. Miocene rotation of Sardinia: New paleomagnetic and geochronological
1033 constraints and geodynamic implications. *Earth and Planetary Science Letters*, 258(3-
1034 4), 359-377. <https://doi.org/10.1016/j.epsl.2007.02.003>.

1035 Ghosh, P., Adkins, J., Affek, H., Balta, B., Guo, W., Schauble, E. A., Schrag, D., and Eiler, J.
1036 M. 2006. ^{13}C - ^{18}O bonds in carbonate minerals: a new kind of paleothermometer.
1037 *Geochimica et Cosmochimica Acta*, 70(6), 1439-1456.
1038 <https://doi.org/10.1016/j.gca.2005.11.014>

1039 Goedert, J., Amiot, R., Arnaud-Godet, F., Cuny, G., Fourel, F., Hernandez, J. A., Pedreira-
1040 Segade, U., and Lecuyer, C. 2017. Miocene (Burdigalian) seawater and air
1041 temperatures estimated from the geochemistry of fossil remains from the Aquitaine

1042 Basin, France. *Palaeogeography, Palaeoclimatology, Palaeoecology*, 481, 14-28.
1043 <https://doi.org/10.1016/j.palaeo.2017.04.024>.

1044 Goldner, A., Herold, N., and Huber, M. 2014. The Challenge of Simulating the Warmth of the
1045 Mid-Miocene Climatic Optimum in CESM1. *Climate of the Past*, 10, 523-536.
1046 <https://doi.org/10.5194/cp-10-523-2014>.

1047 Grossman, E. L. 2012. Applying oxygen isotope paleothermometry in deep time. *The*
1048 *Paleontological Society Papers*, 18, 39-68.
1049 <https://doi.org/10.1017/S1089332600002540>.

1050 Gueguen, E., Doglioni, C., and Fernandez, M. 1998. On the post-25 Ma geodynamic
1051 evolution of the western Mediterranean. *Tectonophysics*, 298(1-3), 259-269.
1052 [https://doi.org/10.1016/S0040-1951\(98\)00189-9](https://doi.org/10.1016/S0040-1951(98)00189-9).

1053 Hamon, Y., Santerre, Y., Granjeon, D., Conesa, G., and Borgomano, J. 2013. Early diagenesis
1054 in meteoric versus brackish environments: Example of the Late Oligocene-Early
1055 Miocene, littoral, mixed sedimentary succession of Carry-Le-Rouet (southeastern
1056 France). *Bulletin de la Société géologique de France*, 184(6), 601-620.
1057 <https://doi.org/10.2113/gssgfbull.184.6.601>.

1058 Hannig, J., and Marron, J. S. 2006. Advanced distribution theory for SiZer. *Journal of the*
1059 *American Statistical Association*, 101(474), 484-499.

1060 Harzhauser, M., Piller, W. E., Müllegger, S., Grunert, P., and Micheels, A. 2011. Changing
1061 seasonality patterns in Central Europe from Miocene Climate Optimum to Miocene
1062 Climate Transition deduced from the *Crassostrea* isotope archive. *Global and*
1063 *Planetary Change*, 76(1-2), 77-84. <https://doi.org/10.1016/j.gloplacha.2010.12.003>.

1064 Henkes, G. A., Passey, B. H., Wanamaker Jr, A. D., Grossman, E. L., Ambrose Jr, W. G., and
1065 Carroll, M. L. 2013. Carbonate clumped isotope compositions of modern marine

1066 mollusk and brachiopod shells. *Geochimica et Cosmochimica Acta*, 106, 307-325.
1067 <https://doi.org/10.1016/j.gca.2012.12.020>.

1068 van Hinsbergen, D. J., Torsvik, T. H., Schmid, S. M., Mañenco, L. C., Maffione, M., Vissers,
1069 R. L., Gürer, D., and Spakman, W. 2019. Orogenic architecture of the Mediterranean
1070 region and kinematic reconstruction of its tectonic evolution since the Triassic.
1071 *Gondwana Research*. <https://doi.org/10.1016/j.gr.2019.07.009>.

1072 Holbourn, A., Kuhnt, W., Schulz, M., and Erlenkeuser, H. 2005. Impacts of orbital forcing
1073 and atmospheric carbon dioxide on Miocene ice-sheet expansion. *Nature*, 438(7067),
1074 483. <https://doi.org/10.1038/nature04123>.

1075 Holbourn, A., Kuhnt, W., Kochhann, K. G., Andersen, N., and Sebastian Meier, K. J. 2015.
1076 Global perturbation of the carbon cycle at the onset of the Miocene Climatic
1077 Optimum. *Geology*, 43(2), 123-126. <https://doi.org/10.1130/G36317.1>.

1078 Holmes, A. 1965. *Principles of Physical Geology*. 2nd edn., Thomas Nelson, London, 1288 pp.

1079 Huang, K. F., You, C. F., Chung, C. H., and Lin, I. T. 2011. Nonhomogeneous seawater Sr
1080 isotopic composition in the coastal oceans: A novel tool for tracing water masses and
1081 submarine groundwater discharge. *Geochemistry, Geophysics, Geosystems*, 12(5).
1082 <https://doi.org/10.1029/2010GC003372>.

1083 Huyghe, D., Mouthereau, F., and Emmanuel, L. 2012. Oxygen isotopes of marine mollusc
1084 shells record Eocene elevation change in the Pyrenees. *Earth and Planetary Science*
1085 *Letters*, 345, 131-141. <https://doi.org/10.1016/j.epsl.2012.06.035>.

1086 Huyghe, D., Lartaud, F., Emmanuel, L., Merle, D., and Renard, M. 2015. Palaeogene climate
1087 evolution in the Paris Basin from oxygen stable isotope ($\delta^{18}\text{O}$) compositions of marine
1088 molluscs. *Journal of the Geological Society*, 172(5), 576-587.
1089 <https://doi.org/10.1144/jgs2015-016>.

1090 Huyghe, D., de Raféllis, M., Ropert, M., Mouchi, V., Emmanuel, L., Renard, M., and Lartaud,
1091 F. 2019. New insights into oyster high-resolution hinge growth patterns. *Marine*
1092 *biology*, 166(4), 48. <https://doi.org/10.1007/s00227-019-3496-2>.

1093 Ingram, B. L., and Sloan, D. 1992. Strontium isotopic composition of estuarine sediments as
1094 paleosalinity-paleoclimate indicator. *Science*, 255(5040), 68-72.
1095 <https://doi.org/10.1126/science.255.5040.68>.

1096 Ivany, L. C., Patterson, W. P., and Lohmann, K. C. 2000. Cooler winters as a possible cause
1097 of mass extinctions at the Eocene/Oligocene boundary. *Nature*, 407(6806), 887.
1098 <https://doi.org/10.1038/35038044>.

1099 Jiménez-Moreno, G., and Suc, J. P. 2007. Middle Miocene latitudinal climatic gradient in
1100 Western Europe: evidence from pollen records. *Palaeogeography, Palaeoclimatology,*
1101 *Palaeoecology*, 253(1-2), 208-225. <https://doi.org/10.1016/j.palaeo.2007.03.040>.

1102 Jiménez-Moreno, G., Fauquette, S., and Suc, J. P. 2010. Miocene to Pliocene vegetation
1103 reconstruction and climate estimates in the Iberian Peninsula from pollen data. *Review*
1104 *of Palaeobotany and Palynology*, 162(3), 403-415.
1105 <https://doi.org/10.1016/j.revpalbo.2009.08.001>.

1106 Jolivet, L., Augier, R., Robin, C., Suc, J. P., and Rouchy, J. M. 2006. Lithospheric-scale
1107 geodynamic context of the Messinian salinity crisis. *Sedimentary geology*, 188, 9-33.
1108 <https://doi.org/10.1016/j.sedgeo.2006.02.004>.

1109 Kirby, M. X., Soniat, T. M., and Spero, H. J. 1998. Stable isotope sclerochronology of
1110 Pleistocene and Recent oyster shells (*Crassostrea virginica*). *Palaios*, 13(6), 560-569.
1111 <https://doi.org/10.2307/3515347>.

1112 Klein, R. T., K. C. Lohmann, and C. W. Thayer. 1996. Sr/Ca and $^{13}\text{C}/^{12}\text{C}$ ratios in skeletal
1113 calcite of *Mytilus trossulus*: Covariation with metabolic rate, salinity, and carbon

1114 isotopic composition of seawater, *Geochim. Cosmochim. Acta*, 60, 4207– 4221.
1115 [https://doi.org/10.1016/S0016-7037\(96\)00232-3](https://doi.org/10.1016/S0016-7037(96)00232-3).

1116 Kocsis, L., Vennemann, T. W., Fontignie, D., Baumgartner, C., and Montanari, A. 2008.
1117 Oceanographic and climatic evolution of the Miocene Mediterranean deduced from
1118 Nd, Sr, C, and O isotope compositions of marine fossils and sediments.
1119 *Paleoceanography*, 23, PA4211. <https://doi.org/10.1029/2007PA001540>.

1120 Kocsis, L., Vennemann, T. W., Hegner, E., Fontignie, D., and Tütken, T. 2009. Constraints on
1121 Miocene oceanography and climate in the Western and Central Paratethys: O-, Sr-,
1122 and Nd-isotope compositions of marine fish and mammal remains. *Palaeogeography*,
1123 *Palaeoclimatology*, *Palaeoecology*, 271(1-2), 117-129.
1124 <https://doi.org/10.1016/j.palaeo.2008.10.003>.

1125 Lartaud, F., De Rafé́lis, M., Ropert, M., Emmanuel, L., Geairon, P., and Renard, M. 2010. Mn
1126 labelling of living oysters: artificial and natural cathodoluminescence analyses as a
1127 tool for age and growth rate determination of *C. gigas* (Thunberg, 1793) shells.
1128 *Aquaculture*, 300(1-4), 206-217. <https://doi.org/10.1007/s10347-009-0196-2>.

1129 Langlet, D., Alunno-Bruscia, M., Rafé́lis, M., Renard, M., Roux, M., Schein, E., and Buestel,
1130 D. 2006. Experimental and natural cathodoluminescence in the shell of *Crassostrea*
1131 *gigas* from Thau lagoon (France): ecological and environmental implications. *Marine*
1132 *Ecology Progress Series*, 317, 143-156. <https://doi.org/10.3354/meps317143>.

1133 Lartaud, F., Langlet, D., De Rafelis, M., Emmanuel, L., and Renard, M. 2006. Mise en
1134 évidence de rythmicité saisonnière dans la coquille des huîtres fossiles *Crassostrea*
1135 *aginensis* Tournouer, 1914 (Aquitaniens) et *Ostrea bellovacina* Lamarck, 1806
1136 (Thané́tien). Approche par cathodoluminescence et par sclérochronologie. *Geobios*,
1137 39(6), 845-852. <https://doi.org/10.1016/j.geobios.2005.11.001>.

- 1138 Lear, C. H., Bailey, T. R., Pearson, P. N., Coxall, H. K., and Rosenthal, Y. 2008. Cooling and
1139 ice growth across the Eocene-Oligocene transition. *Geology*, 36(3), 251-254.
1140 <https://doi.org/10.1130/G24584A.1>.
- 1141 Lear, C. H., Coxall, H. K., Foster, G. L., Lunt, D. J., Mawbey, E. M., Rosenthal, Y., Sosdian,
1142 S. M., Thomas, E., and Wilson, P. A. 2015. Neogene ice volume and ocean
1143 temperatures: Insights from infaunal foraminiferal Mg/Ca paleothermometry.
1144 *Paleoceanography*, 30(11), 1437-1454. <https://doi.org/10.1002/2015PA002833>.
- 1145 Lecuyer, C., Grandjean, P., Paris, F., Robardet, M., and Robineau, D. 1996. Deciphering
1146 “temperature” and “salinity” from biogenic phosphates: the $\delta^{18}\text{O}$ of coexisting fishes
1147 and mammals of the Middle Miocene sea of western France. *Palaeogeography,*
1148 *Palaeoclimatology, Palaeoecology*, 126(1-2), 61-74. [https://doi.org/10.1016/S0031-](https://doi.org/10.1016/S0031-0182(96)00070-3)
1149 [0182\(96\)00070-3](https://doi.org/10.1016/S0031-0182(96)00070-3).
- 1150 Levitus, S., and Boyer, T. P. 1994. World ocean atlas 1994. volume 4. temperature (No. PB-
1151 95-270112/XAB; NESDIS-4). National Environmental Satellite, Data, and
1152 Information Service, Washington, DC (United States).
- 1153 Liu, Z., Pagani, M., Zinniker, D., DeConto, R., Huber, M., Brinkhuis, H., Shah, S. R., Leckie,
1154 M., and Pearson, A. 2009. Global cooling during the Eocene-Oligocene climate
1155 transition. *Science*, 323(5918), 1187-1190. <https://doi.org/10.1126/science.1166368>.
- 1156 Marron, J. S., and Chaudhuri, P. 1998. When is a feature really there: the SiZer approach. In
1157 Automatic Target Recognition VIII (Vol. 3371, pp. 306-313). International Society for
1158 Optics and Photonics. <https://doi.org/10.1117/12.323850>.
- 1159 Maurel-ferrandini M. 1976. Reconstitution paléogéographique du Burdigalien du littoral de la
1160 chaîne de la Nerthe et de la région des étangs (Bouches-du-Rhône, France). – PhD
1161 Thesis, University of Provence, Marseille, 87 p.

- 1162 Mawbey, E. M., and Lear, C. H. 2013. Carbon cycle feedbacks during the Oligocene-Miocene
1163 transient glaciation. *Geology*, 41(9), 963-966. <https://doi.org/10.1130/G34422.1>.
- 1164 McArthur, J., and Howarth, R. J. 2004. Strontium isotope stratigraphy. In F. Gradstein, J.
1165 Ogg, and A. Smith (Eds.), *A geologic time scale* (pp. 96–105). Cambridge: Cambridge
1166 University Press.
- 1167 Meckler, A. N., Ziegler, M., Millán, M. I., Breitenbach, S. F., and Bernasconi, S. M. 2014.
1168 Long-term performance of the Kiel carbonate device with a new correction scheme for
1169 clumped isotope measurements. *Rapid Communications in Mass Spectrometry*,
1170 28(15), 1705-1715. <https://doi.org/10.1002/rcm.6949>.
- 1171 Miall, A. D. 1986. Eustatic sea level changes interpreted from seismic stratigraphy: a critique
1172 of methodology with particular reference to the North Sea Jurassic record. *AAPG*
1173 *Bull.* 70, 131-137.
- 1174 Miller, K. G., Wright, J. D., and Fairbanks, R. G. 1991. Unlocking the ice house: Oligocene-
1175 Miocene oxygen isotopes, eustasy, and margin erosion. *Journal of Geophysical*
1176 *Research: Solid Earth*, 96(B4), 6829-6848. <https://doi.org/10.1029/90JB02015>.
- 1177 Mitchell, I. M., Crawford, C. M., and Rushton, M. J. 2000. Flat oyster (*Ostrea angasi*) growth
1178 and survival rates at Georges Bay, Tasmania (Australia). *Aquaculture*, 191(4), 309-
1179 321. [https://doi.org/10.1016/S0044-8486\(00\)00441-5](https://doi.org/10.1016/S0044-8486(00)00441-5).
- 1180 Montanari, A., Carey, S., Coccioni, R., and Deino, A. 1994. Early Miocene tephra in the
1181 Apennine pelagic sequence: an inferred Sardinian provenance and implications for
1182 western Mediterranean tectonics. *Tectonics*, 13(5), 1120-1134.
1183 <https://doi.org/10.1029/94TC00295>.
- 1184 Mosbrugger, V., Utescher, T., and Dilcher, D. L. 2005. Cenozoic continental climatic
1185 evolution of Central Europe. *PNAS*, 102(42), 14964-14969.
1186 <https://doi.org/10.1073/pnas.0505267102>.

1187 Mouchi, V., Briard, J., Gaillot, S., Argant, T., Forest, V., and Emmanuel, L. 2018.
1188 Reconstructing environments of collection sites from archaeological bivalve shells:
1189 Case study from oysters (Lyon, France). *Journal of Archaeological Science: Reports*,
1190 21, 1225-1235. <https://doi.org/10.1016/j.jasrep.2017.10.025>.

1191 Nalin, R., Ghinassi, M., and Basso, D. 2010. Onset of temperate carbonate sedimentation
1192 during transgression in a low-energy siliciclastic embayment (Pliocene of the Val
1193 d'Orcia Basin, Tuscany, Italy). *Facies*, 56(3), 353-368.
1194 <https://doi.org/10.1007/s10347-010-0211-7>.

1195 Nayar, K. G., Panchanathan, D., McKinley, G. H., and Lienhard, J. H. 2014. Surface tension
1196 of seawater. *Journal of Physical and Chemical Reference Data*, 43(4), 043103.
1197 <https://doi.org/10.1063/1.4899037>.

1198 Nemec, W., and Steel, R. J. 1988. What is a fan delta and how do we recognize it. *Fan Deltas:*
1199 *sedimentology and tectonic settings*, 3-13.

1200 Nury, D. 1990. L'Oligocène de Provence méridionale: stratigraphie, dynamique sédimentaire,
1201 reconstitutions paléogéographiques. PhD Thesis, University of Provence, Marseille,
1202 411 p.

1203 Oertli, H. J. 1964. The Venice system for the classification of marine waters according to
1204 salinity. *Publicazioni della Stazione Zoologica di Napoli*, 33, Supplement, p.611.

1205 Ogg, J. G., Ogg, G., and Gradstein, F. M. 2016. A concise geologic time scale: 2016. Elsevier.
1206 <https://doi.org/10.1016/C2009-0-64442-1>.

1207 Ohno, T., and Hirata, T. 2007. Simultaneous determination of mass-dependent isotopic
1208 fractionation and radiogenic isotope variation of strontium in geochemical samples by
1209 multiple collector-ICP-mass spectrometry. *Analytical Sciences*, 23(11), 1275-1280.
1210 <https://doi.org/10.2116/analsci.23.1275>.

1211 Oudet, J., Münch, P., Borgomano, J., Quillevère, F., Melinte-Dobrinescu, M. C., Demory, F.,
1212 Viseur, S., and Corneé, J. J. 2010. Land and sea study of the northeastern golfe du
1213 Lion rifted margin: the Oligocene–Miocene of southern Provence (Nerthe area, SE
1214 France). *Bulletin de la Société géologique de France*, 181(6), 591-607.
1215 <https://doi.org/10.2113/gssgfbull.181.6.591>.

1216 Pagani, M., Arthur, M. A., and Freeman, K. H. 1999. Miocene evolution of atmospheric
1217 carbon dioxide. *Paleoceanography*, 14(3), 273-292.
1218 <https://doi.org/10.1029/1999PA900006>.

1219 Palmer, M. R., and Elderfield, H. 1985. Sr isotope composition of sea water over the past 75
1220 Myr. *Nature*, 314(6011), 526. <https://doi.org/10.1038/314526a0>.

1221 Passey, B. H., and Henkes, G. A. 2012. Carbonate clumped isotope bond reordering and
1222 geospeedometry. *Earth and Planetary Science Letters*, 351, 223-236.
1223 <https://doi.org/10.1016/j.epsl.2012.07.021>.

1224 Paulet, Y. M., Lorrain, A., Richard, J., and Pouvreau, S. 2006. Experimental shift in diet $\delta^{13}\text{C}$:
1225 a potential tool for ecophysiological studies in marine bivalves. *Organic*
1226 *Geochemistry*, 37(10), 1359-1370. <https://doi.org/10.1016/j.orggeochem.2006.01.008>.

1227 Peral, M., Daëron, M., Blamart, D., Bassinot, F., Dewilde, F., Smialkowski, N., Isguder, G.,
1228 Bonnin, J., Jorissen, F., Kissel, C., Michel, E., Vasquez Riveiros, N., and
1229 Waelbroeck, C. 2018. Updated calibration of the clumped isotope thermometer in
1230 planktonic and benthic foraminifera. *Geochimica et Cosmochimica Acta*, 239, 1-16.
1231 <https://doi.org/10.1016/j.gca.2018.07.016>.

1232 Petersen, S. V., Defliese, W. F., Saenger, C., Daëron, M., Huntington, K. W., John, C. M.,
1233 Kelson, J. R., Bernasconi, S. M., Colman, A. S., Klug, T., Olack, G. A., Schauer, A. J.,
1234 Bajnai, D., Bonifacie, M., Breitenbach, S. F. M., Fiebig, J., Fernandez, A. B., Henkes,
1235 G. A., Hodell, D., Katz, A., Kele, S., Lohmann, K. C., Passey, B. H., Peral, M. Y.,

1236 Petrizzo, D. A., Rosenheim, B. E., Tripathi, A., Venturelli, R., Young, E. D., and
1237 Winkelstern, I. Z. 2019. Effects of Improved ¹⁷O Correction on Inter-Laboratory
1238 Agreement in Clumped Isotope Calibrations, Estimates of Mineral-Specific Offsets,
1239 and Temperature Dependence of Acid Digestion Fractionation. *Geochemistry,*
1240 *Geophysics, Geosystems.* 20(7), 3495-3519. <https://doi.org/10.1029/2018GC008127>.

1241 Peucker-Ehrenbrink, B., and Fiske, G. J. 2019. A continental perspective of the seawater
1242 ⁸⁷Sr/⁸⁶Sr record: A review. *Chemical Geology,* 510, 140-165.
1243 <https://doi.org/10.1016/j.chemgeo.2019.01.017>.

1244 Pierre, C. 1999. The oxygen and carbon isotope distribution in the Mediterranean water
1245 masses. *Marine Geology,* 153, 41–55. [https://doi.org/10.1016/S0025-3227\(98\)00090-](https://doi.org/10.1016/S0025-3227(98)00090-5)
1246 5.

1247 Pound, M. J., Haywood, A. M., Salzmann, U., and Riding, J. B. 2012. Global vegetation
1248 dynamics and latitudinal temperature gradients during the Mid to Late Miocene
1249 (15.97–5.33 Ma). *Earth-Science Reviews,* 112(1-2), 1-22.
1250 <https://doi.org/10.1016/j.earscirev.2012.02.005>.

1251 R Core Team 2017. R: A language and environment for statistical computing. R Foundation
1252 for Statistical Computing, Vienna, Austria. <https://www.R-project.org/>.

1253 Railsback, L. B., and Anderson T.F. 1989. Paleoceanographic modeling of temperature-
1254 salinity profiles from stable isotopic data. *Paleoceanography,* v. 4, 801-814.
1255 <https://doi.org/10.1029/PA004i005p00585>.

1256 Randazzo, A. F., Muller, P., Lelkes, G., Juhasz, E., and Hamor, T. 1999. Cool-water
1257 limestones of the Pannonian basinal system, Middle Miocene, Hungary. *Journal of*
1258 *Sedimentary Research,* 69(1), 283-293. <https://doi.org/10.2110/jsr.69.283>.

- 1259 Rehault, J. P., Boillot, G., and Mauffret, A. 1984. The western Mediterranean basin geological
1260 evolution. *Marine Geology*, 55(3-4), 447-477. <https://doi.org/10.1016/0025->
1261 3227(84)90081-1.
- 1262 Reuter, M., Piller, W. E., Brandano, M., and Harzhauser, M. 2013. Correlating Mediterranean
1263 shallow water deposits with global Oligocene–Miocene stratigraphy and oceanic
1264 events. *Global and planetary change*, 111, 226-236.
1265 <https://doi.org/10.1016/j.gloplacha.2013.09.018>.
- 1266 Reynaud, J. Y., Dalrymple, R. W., Vennin, E., Parize, O., Besson, D., and Rubino, J. L. 2006.
1267 Topographic controls on production and deposition of tidal cool-water carbonates,
1268 Uzès Basin, SE France. *Journal of Sedimentary Research*, 76(1), 117-130.
1269 <https://doi.org/10.2110/jsr.2006.07>.
- 1270 Reynaud, J. Y., Vennin, E., Parize, O., Rubino, J. L., and Bourdillon, C. 2012. Incised valleys
1271 and tidal seaways: the example of the Miocene Uzès-Castillon basin, SE France.
1272 *Bulletin de la Société Géologique de France*, 183(5), 471-486.
1273 <https://doi.org/10.2113/gssgfbull.183.5.471>.
- 1274 Riegl, B., and Piller, W. E. 2000. Biostromal coral facies—a Miocene example from the
1275 Leitha Limestone (Austria) and its actualistic interpretation. *Palaios*, 15(5), 399-413.
1276 [https://doi.org/10.1669/0883-1351\(2000\)015<0399:BCFAME>2.0.CO;2](https://doi.org/10.1669/0883-1351(2000)015<0399:BCFAME>2.0.CO;2).
- 1277 Ryland, J. S. 1970. *Bryozoans*. Hutchinson Univ. Library, London, 175.
- 1278 Schauble, E. A., Ghosh, P., and Eiler, J. M. 2006. Preferential formation of ^{13}C – ^{18}O bonds in
1279 carbonate minerals, estimated using first-principles lattice dynamics. *Geochimica et*
1280 *Cosmochimica Acta*, 70(10), 2510-2529. <https://doi.org/10.1016/j.gca.2006.02.011>.
- 1281 Schettino, A., and Turco, E. 2011. Tectonic history of the western Tethys since the Late
1282 Triassic. *Bulletin*, 123(1-2), 89-105. <https://doi.org/10.1130/B30064.1>.

1283 Schöne, B. R., and Giere, O. 2005. Growth increments and stable isotope variation in shells of
1284 the deep-sea hydrothermal vent bivalve mollusk *Bathymodiolus brevior* from the
1285 North Fiji Basin, Pacific Ocean. *Deep Sea Research Part I: Oceanographic Research*
1286 *Papers*, 52(10), 1896-1910. <https://doi.org/10.1016/j.dsr.2005.06.003>.

1287 Schöne, B. R. 2008. The curse of physiology—challenges and opportunities in the
1288 interpretation of geochemical data from mollusk shells. *Geo-Marine Letters*, 28(5-6),
1289 269-285. <https://doi.org/10.1007/s00367-008-0114-6>.

1290 Seibel, M. J., and James, N. P. 2017. Diagenesis of Miocene, incised valley-filling limestones;
1291 Provence, Southern France. *Sedimentary geology*, 347, 21-35.
1292 <https://doi.org/10.1016/j.sedgeo.2016.09.006>.

1293 Shevenell, A. E., Kennett, J. P., and Lea, D. W. 2004. Middle Miocene southern ocean
1294 cooling and Antarctic cryosphere expansion. *Science*, 305(5691), 1766-1770.
1295 <https://doi.org/10.1126/science.1100061>.

1296 Shevenell, A. E., Kennett, J. P., and Lea, D. W. 2008. Middle Miocene ice sheet dynamics,
1297 deep-sea temperatures, and carbon cycling: A Southern Ocean perspective.
1298 *Geochemistry, Geophysics, Geosystems*, 9(2).
1299 <https://doi.org/10.1029/2007GC001736>.

1300 Smith, A. M. 1995. Palaeoenvironmental interpretation using bryozoans: a review. *Geological*
1301 *Society, London, Special Publications*, 83(1), 231-243.
1302 <https://doi.org/10.1144/GSL.SP.1995.083.01.11>.

1303 Sonderegger, D., and Sonderegger, M. D. 2018. Package ‘SiZer’.

1304 Stenzel, H. B. 1971. Oysters. *Treatise on Invertebrate Paleontology, Part N, Bivalvia 3*, N953-
1305 N1224.

- 1306 Steuber, T., Rauch, M., Masse, J. P., Graaf, J., and Malkoč, M. 2005. Low-latitude seasonality
1307 of Cretaceous temperatures in warm and cold episodes. *Nature*, 437(7063), 1341.
1308 <https://doi.org/10.1038/nature04096>.
- 1309 Stolper, D. A., and Eiler, J. M. 2015. The kinetics of solid-state isotope-exchange reactions
1310 for clumped isotopes: A study of inorganic calcites and apatites from natural and
1311 experimental samples. *American Journal of Science*, 315(5), 363-411.
1312 <https://doi.org/10.2475/05.2015.01>.
- 1313 Super, J. R., Thomas, E., Pagani, M., Huber, M., O'Brien, C., and Hull, P. M. 2018. North
1314 Atlantic temperature and pCO₂ coupling in the early-middle Miocene. *Geology*, 46(6),
1315 519-522. <https://doi.org/10.1130/G40228.1>.
- 1316 Surge, D., Lohmann, K. C., and Dettman, D. L. 2001. Controls on isotopic chemistry of the
1317 American oyster, *Crassostrea virginica*: implications for growth patterns.
1318 *Palaeogeography, Palaeoclimatology, Palaeoecology*, 172(3-4), 283-296.
1319 [https://doi.org/10.1016/S0031-0182\(01\)00303-0](https://doi.org/10.1016/S0031-0182(01)00303-0).
- 1320 Taylor, P. D., and James, N. P. 2013. Secular changes in colony-forms and bryozoan
1321 carbonate sediments through geological history. *Sedimentology*, 60(5), 1184-1212.
1322 <https://doi.org/10.1111/sed.12032>.
- 1323 Tempier, C., 1987. Modèle nouveau de mise en place des structures provençales. *Bulletin*
1324 *Société Géologique France* 8 (3), 533–540. <https://doi.org/10.2113/gssgfbull.III.3.533>.
- 1325 Tremblin, M., Hermoso, M., and Minoletti, F. 2016. Equatorial heat accumulation as a long-
1326 term trigger of permanent Antarctic ice sheets during the Cenozoic. *Proceedings of the*
1327 *National Academy of Sciences*, 113(42), 11782-11787.
1328 <https://doi.org/10.1073/pnas.1608100113>.
- 1329 Trezzi, G., Garcia-Orellana, J., Rodellas, V., Masqué, P., Garcia-Solsona, E., and Andersson,
1330 P. S. 2017. Assessing the role of submarine groundwater discharge as a source of Sr to

1331 the Mediterranean Sea. *Geochimica et Cosmochimica Acta*, 200, 42-54.
1332 <https://doi.org/10.1016/j.gca.2016.12.005>.

1333 Ullmann, C. V., Wiechert, U., and Korte, C. 2010. Oxygen isotope fluctuations in a modern
1334 North Sea oyster (*Crassostrea gigas*) compared with annual variations in seawater
1335 temperature: Implications for palaeoclimate studies. *Chemical Geology*, 277(1-2),
1336 160-166. <https://doi.org/10.1016/j.chemgeo.2010.07.019>.

1337 Ullmann, C. V., Campbell, H. J., Frei, R., Hesselbo, S. P., von Strandmann, P. A. P., and
1338 Korte, C. 2013. Partial diagenetic overprint of Late Jurassic belemnites from New
1339 Zealand: Implications for the preservation potential of $\delta^7\text{Li}$ values in calcite fossils.
1340 *Geochimica et Cosmochimica Acta*, 120, 80-96.
1341 <https://doi.org/10.1016/j.gca.2013.06.029>.

1342 Ullmann, C. V., and Korte, C. 2015. Diagenetic alteration in low-Mg calcite from
1343 macrofossils: a review. *Geological Quarterly*, 59(1), 3-20.
1344 <https://doi.org/10.7306/gq.1217>.

1345 Veizer, J., Ala, D., Azmy, K., Bruckschen, P., Buhl, D., Bruhn, F., Carden, G., Diener, A.,
1346 Godderis, Y., Jasper, T., Korte, C., Pawellek, F., Podlaha, O., and Strauss, H. 1999.
1347 $^{87}\text{Sr}/^{86}\text{Sr}$, $\delta^{13}\text{C}$ and $\delta^{18}\text{O}$ evolution of Phanerozoic seawater. *Chemical geology*,
1348 161(1-3), 59-88. [https://doi.org/10.1016/S0009-2541\(99\)00081-9](https://doi.org/10.1016/S0009-2541(99)00081-9).

1349 Weckström, J., Korhola, A., Erästö, P., and Holmström, L. 2006. Temperature patterns over
1350 the past eight centuries in Northern Fennoscandia inferred from sedimentary diatoms.
1351 *Quaternary Research*, 66(1), 78-86. <https://doi.org/10.1016/j.yqres.2006.01.005>.

1352 Widerlund, A., and Andersson, P. S. 2006. Strontium isotopic composition of modern and
1353 Holocene mollusc shells as a palaeosalinity indicator for the Baltic Sea. *Chemical
1354 Geology*, 232(1-2), 54-66. <https://doi.org/10.1016/j.chemgeo.2006.02.010>.

1355 de Winter, N. J. D., Vellekoop, J., Vorsselmans, R., Golreihan, A., Soete, J., Petersen, S. V.,
1356 Meyer, K. W., Casadio, S., Speijer, R. P., Claeys, P. 2018. An assessment of latest
1357 Cretaceous *Pycnodonte vesicularis* (Lamarck, 1806) shells as records for
1358 palaeoseasonality: a multi-proxy investigation. *Climate of the Past*, 14(6), 725-749.
1359 <https://doi.org/10.5194/cp-14-725-2018>.

1360 Yeghicheyan, D., Bossy, C., Le Coz, M. B., Douchet, C., Granier, G., Heimburger, A., Lacan,
1361 F., Lanzanova, A., Rousseau, T., Seidel, J., Tharaud, M., Candaudap, F., Chmeleff, J.,
1362 Cloquet, C., Delpoux, S., Labatut, M., Losno, R., Pradoux, C., Sivry, Y., and Sonke, J.
1363 E. 2013. A compilation of silicon, rare earth element and twenty-one other trace
1364 element concentrations in the natural river water reference material SLRS-5 (NRC-
1365 CNRC). *Geostandards and Geoanalytical Research*, 37(4), 449-467.
1366 <https://doi.org/10.1111/j.1751-908X.2013.00232.x>.

1367 Zachos, J. C., Quinn, T. M., and Salamy, K. A. 1996. High-resolution (104 years) deep-sea
1368 foraminiferal stable isotope records of the Eocene-Oligocene climate transition.
1369 *Paleoceanography*, 11(3), 251-266. <https://doi.org/10.1029/96PA00571>.

1370 Zachos, J., Pagani, M., Sloan, L., Thomas, E., and Billups, K. 2001. Trends, rhythms, and
1371 aberrations in global climate 65 Ma to present. *Science*, 292(5517), 686-693.
1372 <https://doi.org/10.1126/science.1059412>.

1373 Zachos, J. C., Dickens, G. R., and Zeebe, R. E. 2008. An early Cenozoic perspective on
1374 greenhouse warming and carbon-cycle dynamics. *Nature*, 451(7176), 279.
1375 <https://doi.org/10.1038/nature06588>.

1376 Zaky, A. H., Brand, U., Buhl, D., Blamey, N., Bitner, M. A., Logan, A., Gaspard, D., and
1377 Popov, A. 2018. Strontium isotope geochemistry of modern and ancient archives:
1378 tracer of secular change in ocean chemistry. *Canadian Journal of Earth Sciences*,
1379 56(3), 245-264. <https://doi.org/10.1139/cjes-2018-0085>.

1380

1381

1382

1383 TABLE CAPTION

1384 **Table 1** Facies and depositional environments of Carry-Le-Rouet section.

1385

1386 **Table 2** Δ_{47} data for all analyzed samples and conversion to temperature according to Peral et
1387 al. (2018) equation. Analytical errors reported here are derived from the external
1388 reproducibility of carbonate standards (N = 47) and samples (N = 39) within each analytical
1389 session, and conservatively account for the uncertainties in raw Δ_{47} measurements as well as
1390 those associated with the conversion to the “absolute” Δ_{47} reference frame. Local $\delta^{18}\text{O}_{\text{sw}}$
1391 values were calculated using Δ_{47} -derived temperatures and $\delta^{18}\text{O}_{\text{shell}}$ with Anderson and Arthur
1392 (1983) equation. Salinity estimations derives from calculated local $\delta^{18}\text{O}_{\text{sw}}$ values, from which
1393 the $\delta^{18}\text{O}_{\text{sw}}$ of the global ocean (from Billups and Schrag; 2002) has been subtracted, and
1394 Railsback and Anderson (1989) equation based on North Atlantic Ocean.

1395

1396 **Table 3** $^{87}\text{Sr}/^{86}\text{Sr}$ ratios of bulk carbonate and their error bars.

1397

1398 FIGURE CAPTION

1399 **Fig. 1.** Location of the studied outcrops. Absolute ages presented on the left are from Ogg et
1400 al. (2016), along with the correspondence with magnetostratigraphic frame and foraminifera
1401 zonation (C6C to C5A). A. Location of the outcrops on a modern map of the North Western
1402 Mediterranean area. B. Geological map of outcropping latest Chattian to latest Burdigalian
1403 (Oligo-Miocene) formations in the Coastal Nerthe area and their sedimentary units (modified
1404 from Andreieff et al., 1972; Oudet et al., 2010; Demory et al., 2011). The numbers 1 to 8
1405 correspond to logs positions used to build a composite log of over than 80 meters, that is used
1406 in this study. C. Geological map of Burdigalian to earliest Serravallian (Miocene) formations
1407 in the Castillon-Du-Gard sub-basin and their sedimentary units (modified by from Reynaud et
1408 al., 2012). The numbers 1 to 5 correspond to logs positions.

1409

1410 **Fig. 2.** A. Picture representing the location of ligamental area on an oyster shell (modified
1411 from Stenzel, 1971). B. Sections of oyster shells under natural light (LN) and
1412 cathodoluminescence (CL), showing luminescent part in orange (mainly chalky areas) and
1413 non-luminescent to weakly luminescent parts with identifiable seasonal patterns of growths.
1414 Only the non-luminescent to weakly luminescent parts with identifiable seasonal patterns of
1415 growths parts have been sampled for isotopic analyses.

1416

1417 **Fig. 3.** A. Composite log of the Carry-Le-Rouet sedimentary succession with the different
1418 units identified along the log (after Andreieff et al., 1972; Oudet et al., 2010; Demory et al.,
1419 2011), lithologies and marker beds (UR1 to UR4 in red). The position of logs 1 to 8, used to
1420 build this synthetic log, is reported on Fig. 1. B. Outcrop pictures: 1. Transition from
1421 continental conglomerate to marine sandstone in the Chattian Conglomeratic Rouet unit; 2.
1422 Detail of the conglomerate beds eroding sandstones with oyster debris in the Conglomerate

1423 Rouet Unit. 3. Bioclastic carbonate deposits with abundant oyster shells at the transition
1424 between the Brackish Rousset and the Bioclastic Carry units; 4. *Ostrea fimbriata* localized at
1425 the base of the Bioclastic Carry unit; 5. Reefal Unit 4 (UR4) outcropping the Bioclastic Carry
1426 unit in Carry harbor; 6. Detail of the surface topping the UR4 and composed of dense
1427 Poritidae corals preserved in life position; 7. Marls of Tamaris section covered by the
1428 Langhian carbonate deposits; 8. Detail of marls with a low fossil record.

1429

1430 **Fig. 4.** Evolution of bivalve $\delta^{18}\text{O}$ throughout the section of Carry-Le-Rouet (A, Black plain
1431 circles) and Castillon-Du-Gard (B, Grey plain circles). Several microsamplings were realized
1432 per shells (levels where a microsampled oyster has been analyzed are identified by the name
1433 of the shell next to the relevant data) and several shells were analyzed per stratigraphic levels.
1434 Each plotted data represents $\delta^{18}\text{O}$ data acquired in this work, including the multiple $\delta^{18}\text{O}$
1435 measurements realized on some shells, appears on the figure. Analytical uncertainties are
1436 lower than the size of the circles ($\pm 0.08\text{‰}$, see Method section) and cannot be reported for
1437 each data point. Plain squares correspond to $\delta^{18}\text{O}_{\text{shell}}$ measured with clumped isotopes (White
1438 squares correspond to bulk of shell; Red square corresponds to summer part of shell CAR17-
1439 6-33-b; Blue square corresponds to winter part of shell CAR17-6-33). Vertical error bars
1440 reported on two Langhian samples, representing an uncertainty on the stratigraphic position of
1441 the samples, correspond to bulk shells that were gathered from stratigraphic levels next to
1442 each other into a single analysis.

1443

1444 **Fig. 5.** Intra-shells $\delta^{18}\text{O}$ evolution from bivalves recovered from the Carry-Le-Rouet outcrop.
1445 A. CAR17-6-28-a; B. CAR17-6-30top-e; C. CAR17-6-31base-a; D. CAR17-6-33-b; E.
1446 CAR17-6-33-c; F. CAR17-8-43-h; G. CAR17-8-43-i. Corresponding temperatures have been
1447 calculated using the equation of Anderson and Arthur (1983) and a $\delta^{18}\text{O}_{\text{sw}}$ of $-0.66\text{‰}_{\text{VPDB}}$

1448 (Billups and Schrag, 2002) for the Aquitanian (A to E) and of $-0.94 \text{ ‰}_{\text{VPDB}}$ (Billups and
1449 Schrag, 2002) for the Late Burdigalian (F and G). The error bar that applies to $\delta^{18}\text{O}$
1450 measurements corresponds to the analytical reproducibility specified in the Method part, of \pm
1451 0.08 ‰ .

1452

1453

1454 **Fig. 6.** Distribution of $\delta^{18}\text{O}$ values along CAR17-6-33-b umbo obtained from microsampling
1455 (black plain circles). The dotted red and blue lines represent the $\delta^{18}\text{O}$ values of the two
1456 samples recovered from this oyster for Δ_{47} analyses, over the length of the shell corresponding
1457 to minimum $\delta^{18}\text{O}$ values and maximum $\delta^{18}\text{O}$ values, respectively, as described in the text (Part
1458 3.3). The temperature calculated from Δ_{47} ($T(\Delta_{47})$) is reported for these two samples. The
1459 error bar that applies to $\delta^{18}\text{O}$ measurements corresponds to the analytical reproducibility
1460 specified in the Method part, of $\pm 0.08 \text{ ‰}$.

1461

1462 **Fig. 7.** Comparison of geochemical data from bivalve shells obtained in this work, with the
1463 results of the applied statistical treatment (SiZer Map: $0.1 < h < 10$ Myrs ; Blue: significant
1464 increase; Red: significant decrease; Grey: No significant; White: No data), with the benthic
1465 foraminifera $\delta^{18}\text{O}$ global record (Zachos et al., 2008). Black plain circles correspond to
1466 bivalve $\delta^{18}\text{O}$ values for the Carry-Le-Rouet section and Grey plain circles correspond to
1467 bivalve $\delta^{18}\text{O}$ values from Castillon-Du-Gard. Smoothed black curves and their grey envelope
1468 on foraminifera $\delta^{18}\text{O}$ global record and on our bivalve $\delta^{18}\text{O}$ values are realized using
1469 *locally.weighted.polynomial* function (the confidence intervals are created using the row-wise
1470 method of Hannig and Marron, 2006) of SiZer Package (R software) with a bandwidth “h” at 1
1471 Ma for both curves.

1472

1473 **Fig. 8.** A. Comparison between $\delta^{18}\text{O}$ -derived temperatures and Δ_{47} -derived Temperatures.
1474 $\delta^{18}\text{O}$ -derived temperatures are calculated using the $\delta^{18}\text{O}_{\text{sw}}$ from Billups and Scharg (2002) and
1475 the equation of Anderson and Arthur (1983) as described in the text, Sections 5.1 and 5.2.1.
1476 Black plain circles correspond to Carry-Le-Rouet section; Grey plain circles correspond to
1477 Castillon-Du-Gard Section. Vertical error bars reported on 2 bulk shells, representing an
1478 uncertainty on the stratigraphic position of the samples, correspond to bulk shells that were
1479 gathered from stratigraphic levels next to each other into a single analysis. Black smoothed
1480 curve and associated grey interval have been realized using the *locally.weighted.polynomial*
1481 function with a bandwidth “h” at 1 Ma. Δ_{47} -derived mean annual temperatures are estimated
1482 from clumped isotope analyses bulk shells using the equation of Peral et al. (2018): Orange
1483 squares: mean annual temperatures; Red square: summer seawater (CAR17-6-33-b); Blue
1484 square: winter seawater temperatures (CAR17-6-33-b). Vertical error bars as for $\delta^{18}\text{O}$ -derived
1485 temperatures. B. Evolution of local $\delta^{18}\text{O}_{\text{sw}}$ calculated from $\delta^{18}\text{O}_{\text{shell}}$ and Δ_{47} -derived
1486 temperatures using Anderson and Arthur (1983) equation (see section 5.2.3 for further detail)
1487 C. Global $\delta^{18}\text{O}_{\text{sw}}$ curve, is from Billups and Schrag (2002). The shaded areas reported on this
1488 curve highlight the portions of the curve selected to calculate the average $\delta^{18}\text{O}_{\text{sw}}$ value of the
1489 global ocean for the three periods for which coupled Δ_{47} - $\delta^{18}\text{O}$ analyses have been performed
1490 on bivalves, with a minimum of 3 data of the curve gathered for the calculation. D. Salinity
1491 estimations are calculated using Railsback and Anderson (1989) equation based on North
1492 Atlantic Ocean and local $\delta^{18}\text{O}_{\text{sw}}$ values from which global ocean $\delta^{18}\text{O}_{\text{sw}}$ value has been
1493 subtracted (see section 5.2.3 for further detail) E. Bivalve $^{87}\text{Sr}/^{86}\text{Sr}$ evolution (white squares)
1494 compared to the $^{87}\text{Sr}/^{86}\text{Sr}$ of the global ocean (black line; McArthur and Howarth, 2004) with
1495 the two red dashed lines showing the variability of ± 50 ppm recorded in the modern ocean
1496 (El Meknassi et al., 2018), and compared to published planktonic foraminifera (Cornacchia et

1497 al., 2018) and mixed fossils (Kocsis et al., 2008) $^{87}\text{Sr}/^{86}\text{Sr}$ from the North Western
1498 Mediterranean Sea.

1499

1500 **Fig. 9.** A. $\delta^{18}\text{O}_{\text{shell}}$ values versus Δ_{47} -derived temperatures measured with clumped isotopes.

1501 B. Local $\delta^{18}\text{O}_{\text{sw}}$ values calculated with Anderson and Arthur (1983) equation versus $\delta^{18}\text{O}_{\text{shell}}$

1502 values measured with clumped isotopes.

1503

Figure 1

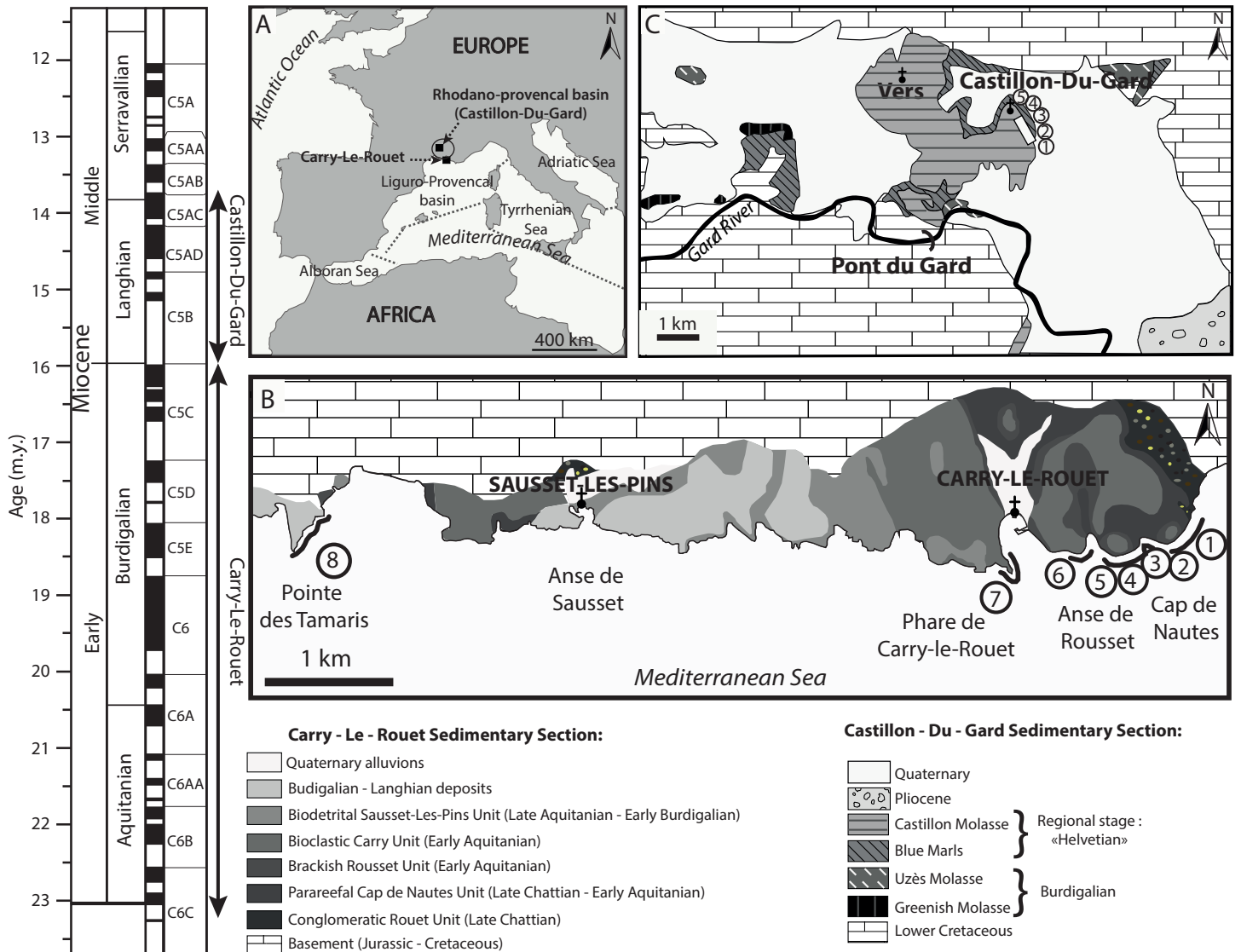


Figure 2

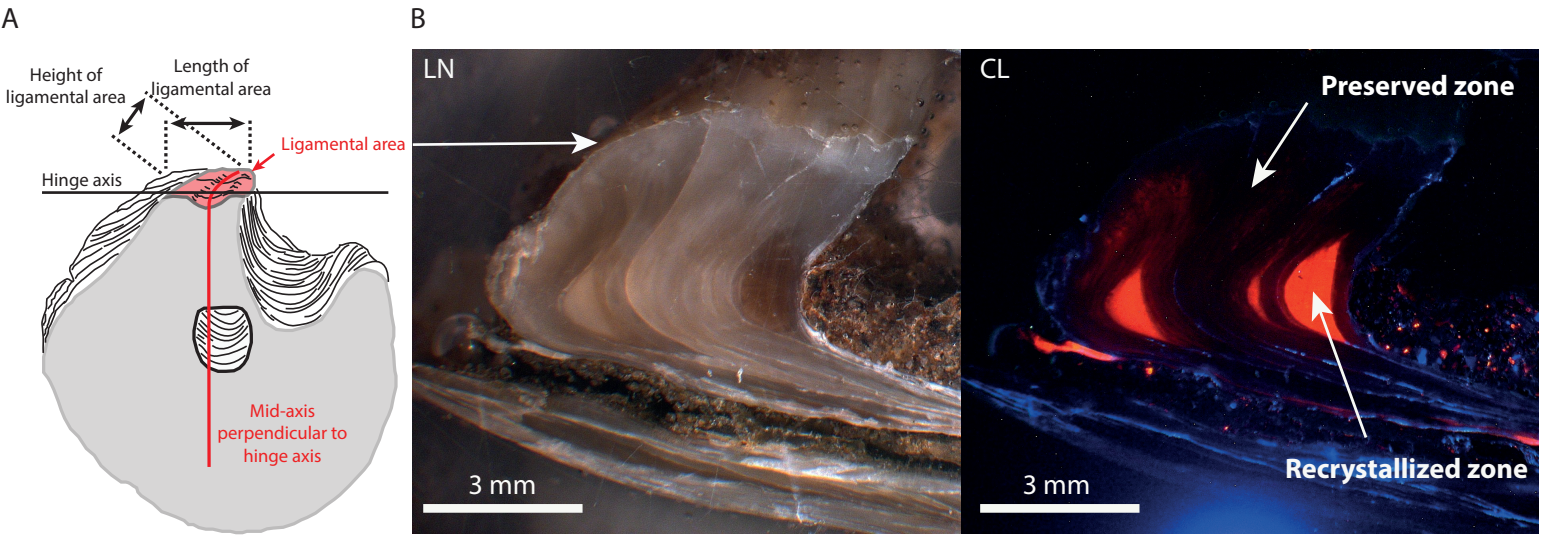


Figure 4

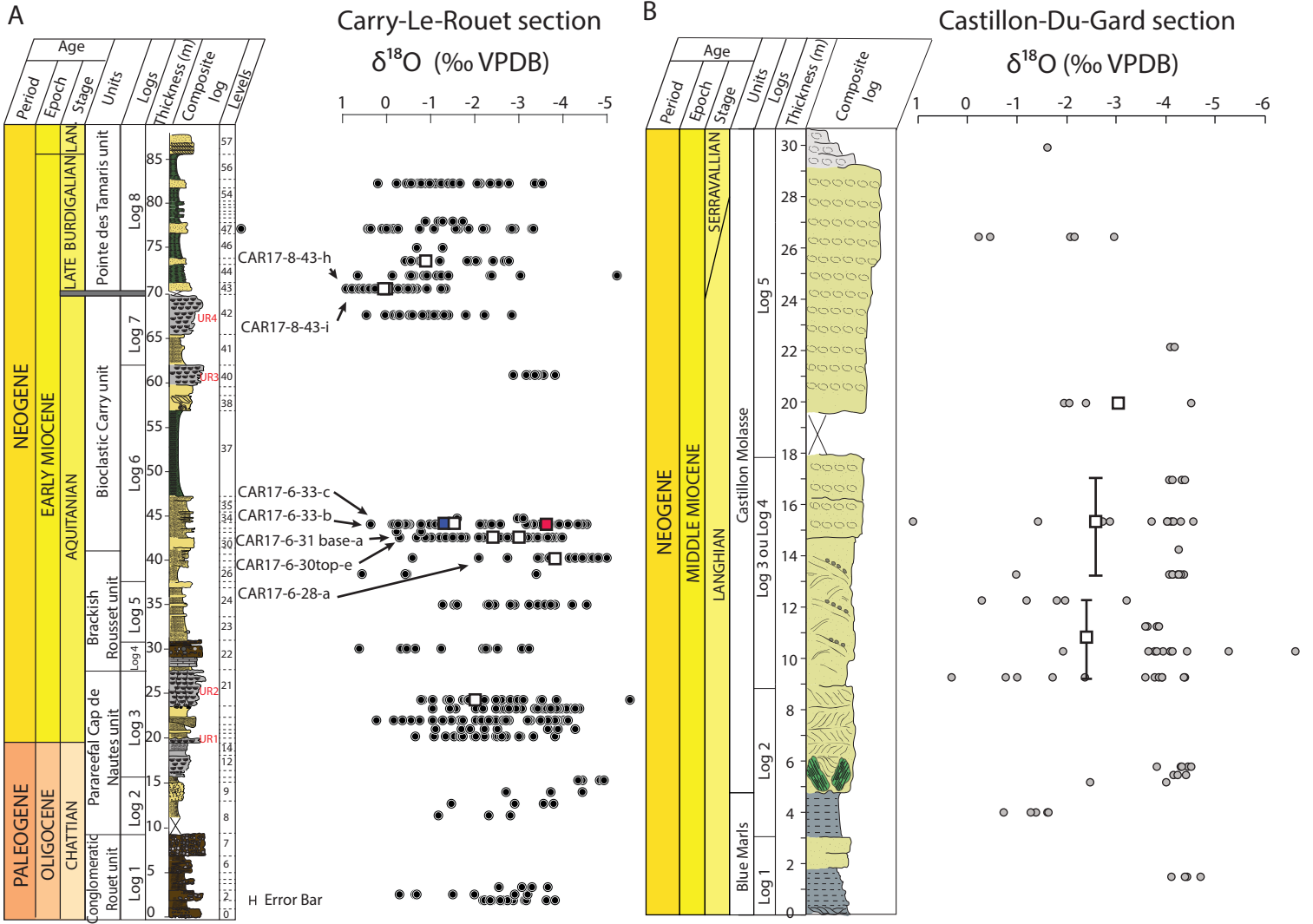


Figure 5

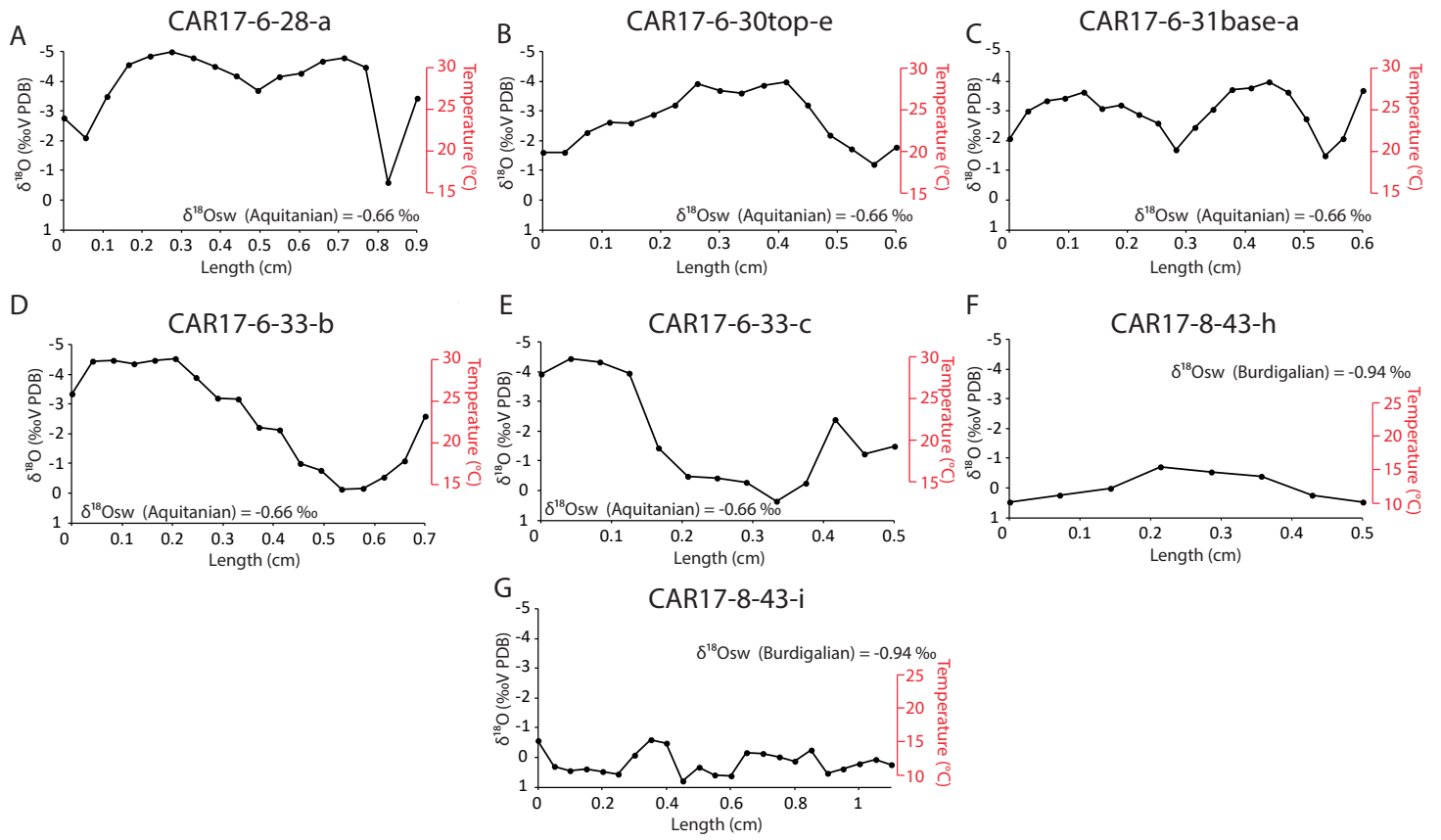


Figure 6

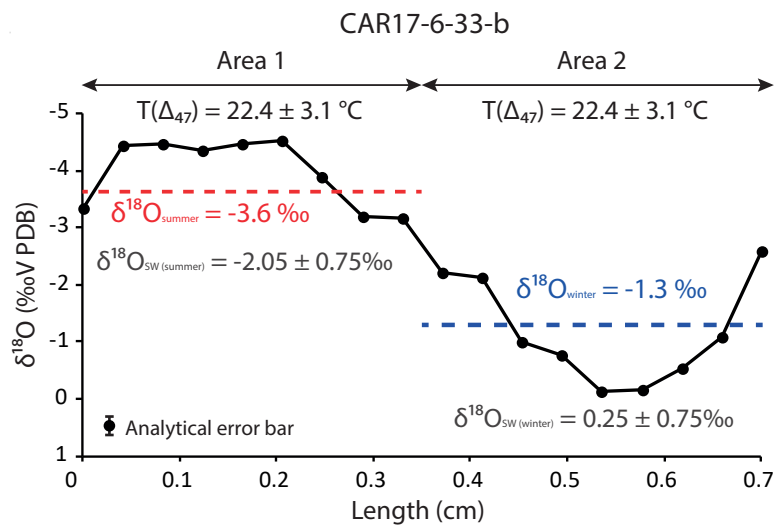


Figure 7

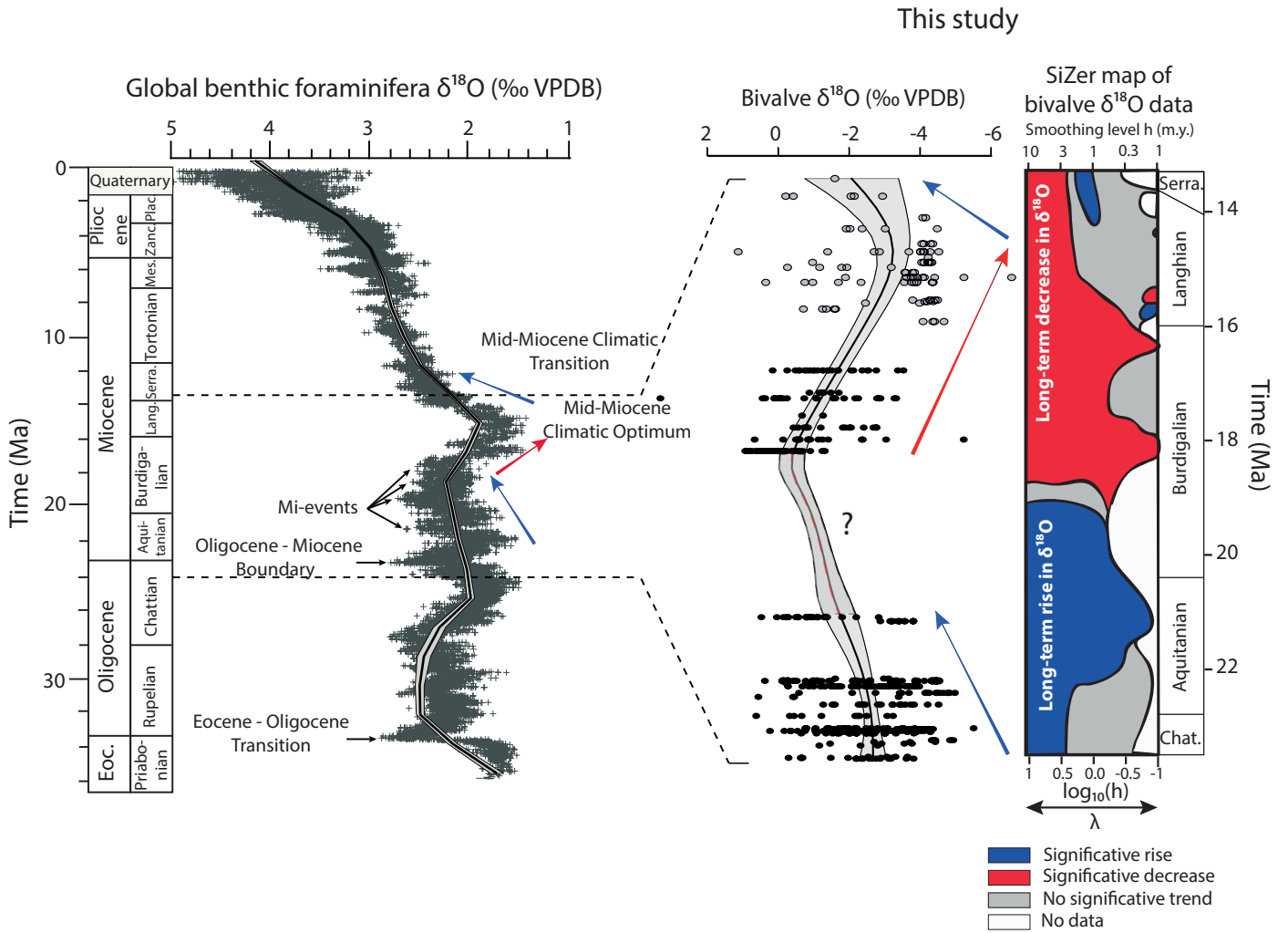


Figure 8

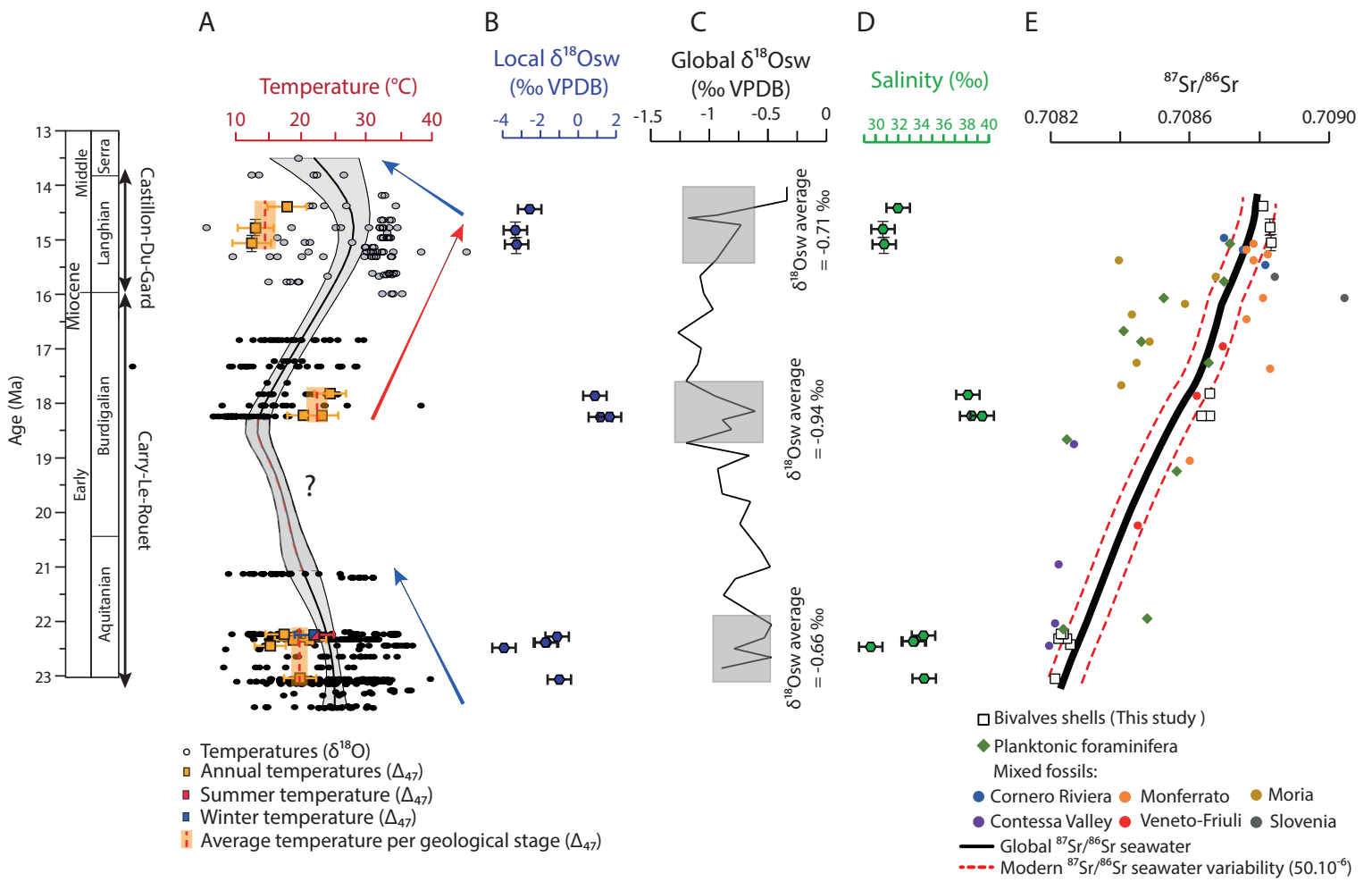


Figure 9

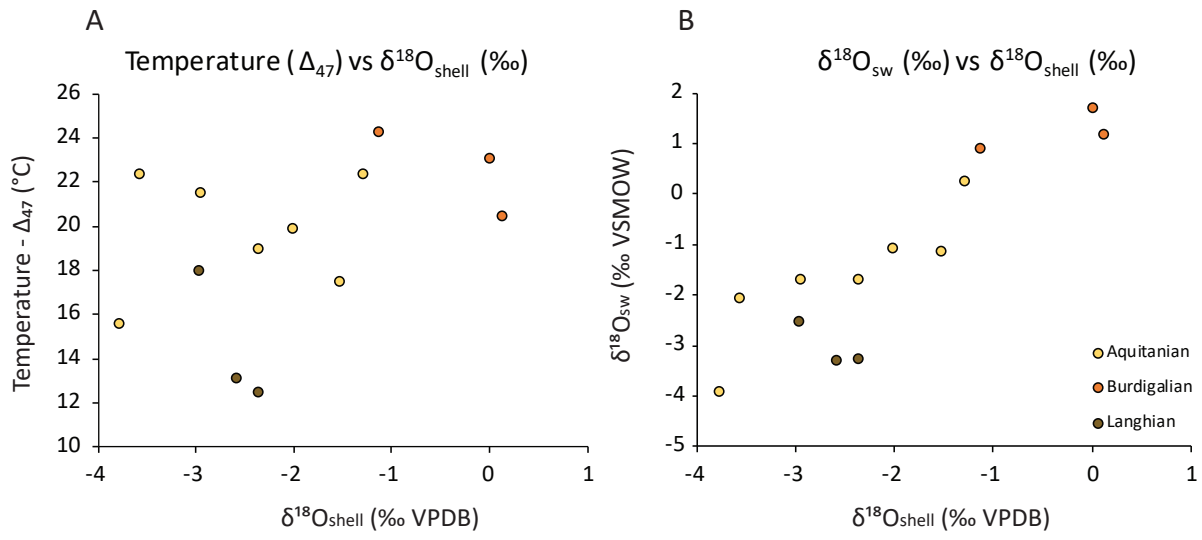


Table 1

Facies	Non-biotic elements		Biotic components	Matrix	Sedimentary structures	Environments
A1. Marls to fine siltstones	Rhizo-concretion, root traces			Clayey silts		Palaeosoils, Floodplain
A2. Conglomerates	Monogenic	Clasts source: Rudist Limestone (Barremian of the Nerthe)		Heterogeneous and clast-supported conglomerates with a sandstone matrix	Erosional base of decimetric to meter large channels	Fluviatile
	Poligenic	Clasts source : Rudist Limestones (Barremian of the Nerthe) and Paleozoic rocks				
A3. Conglomerates	Polygenic conglomerate with clasts composed of Rudist Limestones (Barremian of the Nerthe) and Paleozoic rocks		Rare bivalves and gastropods			Proximal deltaic domain
A4. Sandstones	Quartz grains, feldspath		Rare bivalves and gastropods	Calcareous sandstone	Continuous cm-thick beds intercalated with oyster and bioturbated sandstones	Distal deltaic lobes, transitional continental to marine
B1. Sandstones with conglomerates	Sandstones with quartz		Common bivalves, gastropods and barnacles	Fine grain sandstones	Planar stratification Bioturbation	Upper shoreface
B2. Fine to coarse sandstones	Quartz grains		Abundant bivalves Common gastropods Rare wood fragments and bryozoans	Fine grain sandstones	Megaripples, HCS (Hummocky cross stratification), Convolute beds, Bioturbation	Lower shoreface
C. Siltstones to marls	Quartz grains		Common wood fragments and foraminifera Rare bivalves	Silt and Marls	Bioturbation (<i>Thalassinoides</i> / <i>Planolites</i>), HCS	Lagoon, protected environments
D1. Bioclastic packstones	Quartz grains		Abundant bivalves, gasteropods and corals Common bryozoans and echinoids	Broken bioclastic grains and micritic matrix	Bioturbation	Upper to lower shoreface
D2. Coral-rich floatstones to framestones	Floatstones	Reworked corals, and fragmented bioclasts	Abundant corals Common bivalves, gasteropods and bryozoans		Bioturbation, bioerosion, lenticular bioclastic accumulation and sigmoid reefal units	Lower shoreface
	Framestones	In situ corals, embedded in a bioclastic matrix				

Table 2.

Age (m.y)	Sample	N	Seasonality	$\delta^{18}\text{O}_{\text{shell}}$ (‰V-PDB)	Δ_{47} (‰, $\pm 1 \sigma_E$)	T (°C)	$\delta^{18}\text{O}_{\text{sw}}$ calculated (‰V-SMOW)	$\delta^{18}\text{O}_{\text{sw}}$ (Billups and Schrag, 2002) (‰V-PDB)	Salinity (‰)
22.9	CAR17_4_21A_a_B1	3	Bulk	-2.02	0.6903 ± 0.0093	19.9 ± 2.8	-1.06 ± 0.68	-0.66	34.3 ± 1.1
22.3	CAR17_6_28_a_B1	3	Bulk	-3.79	0.705 ± 0.0095	15.6 ± 2.7	-3.9 ± 0.65	-0.66	29.6 ± 1.1
22.2	CAR17_6_30TOP_B1	2	Bulk	-2.37	0.6934 ± 0.0097	19 ± 2.9	-1.68 ± 0.7	-0.66	33.3 ± 1.2
22.2	CAR17_6_31BASE_a_B1	3	Bulk	-2.96	0.6852 ± 0.0093	21.5 ± 2.9	-1.67 ± 0.7	-0.66	33.3 ± 1.2
22.1	CAR17_6_33_b_S1	3	Summer	-3.58	0.6821 ± 0.01	22.4 ± 3.1	-2.05 ± 0.75	-0.66	32.7 ± 1.3
22.1	CAR17_6_33_b_W1	3	Winter	-1.3	0.6823 ± 0.0099	22.4 ± 3.1	0.25 ± 0.75	-0.66	36.5 ± 1.3
22.1	CAR17_6_33_c_B1	3	Bulk	-1.53	0.6986 ± 0.01	17.5 ± 3	-1.14 ± 0.72	-0.66	34.2 ± 1.2
18.1	CAR17_8_43_h_B1	3	Bulk	0	0.6801 ± 0.0093	23.1 ± 2.9	1.71 ± 0.70	-0.94	39.4 ± 1.2
18.1	CAR17_8_43_i_B1	3	Bulk	0.12	0.6882 ± 0.0093	20.5 ± 2.8	1.19 ± 0.68	-0.94	38.5 ± 1.1
17.7	CAR17_8_45_a_B1	3	Bulk	-1.13	0.6762 ± 0.0093	24.3 ± 2.9	0.9 ± 0.70	-0.94	38.1 ± 1.2
14.9	CDG18_3&4_BASE_B1	3	Bulk	-2.37	0.7157 ± 0.0099	12.5 ± 2.8	-3.25 ± 0.68	-0.71	30.8 ± 1.1
14.6	CDG18_3&4_TOP_B1	3	Bulk	-2.59	0.7137 ± 0.0099	13.1 ± 2.8	-3.3 ± 0.68	-0.71	30.7 ± 1.1
14.2	CDG18_5_1_B1	3	Bulk	-2.98	0.6968 ± 0.0098	18 ± 2.9	-2.52 ± 0.70	-0.71	32 ± 1.2

Table 3

Age (m.y)	Sample	Nature	$^{87}\text{Sr}/^{86}\text{Sr}$	+ 2 σ_E
22.9	CAR17_4_21A_a_B1	Bulk	0.708255	0.000005
22.3	CAR17_6_28_a_B1	Bulk	0.708299	0.000007
22.2	CAR17_6_30TOP_B1	Bulk	0.708289	0.000005
22.2	CAR17_6_31BASE_a_B1	Bulk	0.708266	0.000005
22.1	CAR17_6_33_b_B1	Bulk	0.708228	0.000005
22.1	CAR17_6_33_c_B1	Bulk	0.708271	0.000009
18.1	CAR17_8_43_h_B1	Bulk	0.708696	0.000005
18.1	CAR17_8_43_i_B1	Bulk	0.708673	0.000006
17.7	CAR17_8_45_a_B1	Bulk	0.708695	0.000005
14.9	CDG18_3&4_BASE_B1	Bulk	0.708873	0.000005
14.6	CDG18_3&4_TOP_B1	Bulk	0.708868	0.000006
14.2	CDG18_5_1_B1	Bulk	0.708849	0.000005